Shallow deformation on the Kirby Hills fault, Sacramento–San Joaquin Delta, California (USA), revealed from high-resolution seismic reflection data and coring in a fluvial system

Shannon Klotsko[1,2,3], Jillian Maloney[2,3], and Janet Watt[4]

[1]Department of Earth and Ocean Sciences, University of North Carolina Wilmington, Wilmington, North Carolina 28402, USA
[2]Center for Marine Science, University of North Carolina Wilmington, Wilmington, North Carolina 28402, USA
[3]Department of Geological Sciences, San Diego State University, San Diego, California 92182, USA
[4]U.S. Geological Survey Pacific Coastal and Marine Science Center, Santa Cruz, California 94025, USA

ABSTRACT

The Sacramento–San Joaquin Delta (Delta) in California (USA) is an important part of the state's freshwater system and is also a major source of agricultural and natural resources. However, the Delta is traversed by a series of faults that make up the easternmost part of the San Andreas fault system at this latitude and pose seismic hazard to this region. In this study, we use new high-resolution chirp subbottom data[1] to map and characterize the shallow expression of the Kirby Hills fault, where it has been mapped to cross the Sacramento River at the western extent of the Delta. The fault is buried here, but we document a broad zone of deformation associated with the eastern strand of the fault that changes in character, along strike, across ~600 m of the river channel. Radiocarbon dates from sediment cores collected in the Sacramento River provide some minimum constraints on the age of deformation. We do not observe evidence of the western strand as previously mapped. We also discuss difficulties of conducting a paleoseismologic study in a fluvial environment.

■ INTRODUCTION

The Kirby Hills fault zone (Fig. 1) cuts through the western extent of the Sacramento–San Joaquin Delta (Delta), east of San Francisco Bay (California, USA), in the middle of the urban-rural transition. The Delta is the backbone of California's water conveyance system with ~50% of the freshwater used by the state flowing through it (Lund et al., 2007). It is also a major agricultural area and important ecological system, supporting more than 750 species of plants and animals (Delta Stewardship Council, 2013). Because of this, the Delta's islands and tracts are protected by more than 1700 km of human-made levees (Ingebritsen

---

[1]Chirp data are archived at the Marine Geoscience Data System and can be accessed through the Academic Seismic Portal (https://www.marine-geo.org/collections/#!/collection/Seismic#summary). The data sets have DOIs: https://doi.org/10.26022/IEDA/330931 and https://doi.org/10.26022/IEDA/330932. Sediment cores are archived at the USGS Pacific Coastal and Marine Science Center.

Shannon Klotsko https://orcid.org/0000-0002-8485-0293

and Ikehara, 1999; Suddeth et al., 2010). In the event of a substantial earthquake, ground shaking could cause levee failure from liquefaction of the underlying sediments (Mount and Twiss, 2005; Suddeth et al., 2010), which would result in the contamination of freshwater and the destruction of valuable agricultural land and habitats (CALFED Bay-Delta Program, 2000; Mount and Twiss, 2005; Suddeth et al., 2010). The Kirby Hills fault (Figs. 1 and 2) is an active fault with most of its measured seismicity below M_L 4 (Weber-Band et al., 1997; Fig. 3); however, it could potentially generate an earthquake as large as moment magnitude (M) 6.7 (WGCEP Thrust Fault Subgroup, 1999), potentially large enough to cause levee failure.

The Kirby Hills fault is primarily buried or blind, with some surficial geomorphic expression on land (Unruh and Sundermann, 2006). Within the Sacramento River, the fault tip is deeper than 75 m, but exact depth is unknown because the fault plane is not resolved in deeper-penetration seismic data (Parsons et al., 2002). Previous work (Parsons et al., 2002) identified deformation of the Sacramento River floor associated with the Kirby Hills fault, indicating relatively recent activity near the surface. To better characterize the shallow expression of deformation associated with the Kirby Hills fault and constrain the age of deformation, we resurveyed this area (Fig. 2) with a higher-resolution seismic reflection system (chirp subbottom profiler) and collected sediment cores. Our results highlight the importance of submarine methodologies for paleoseismic studies in developed areas but also the limitations of these methods in a fluvial system.

■ GEOLOGIC BACKGROUND

The Kirby Hills fault, also referred to as the Rio Vista fault (USGS and CGS, 2020), is a NNE-SSW–striking fault located within the former Great Valley forearc basin and represents the western boundary of the Rio Vista Basin (Fig. 1), a subbasin of the regional Sacramento Basin (Cherven, 1983; Krug et al., 1992). The Kirby Hills fault extends 53 km from the town of Vacaville in the north to the city of Pittsburg in the south (Fig. 1; USGS and CGS, 2020; Graymer et al., 2006). The fault has been characterized as a reactivated structure that was initiated during the Eocene as a normal fault (Krug et al., 1992; MacKevett, 1992).
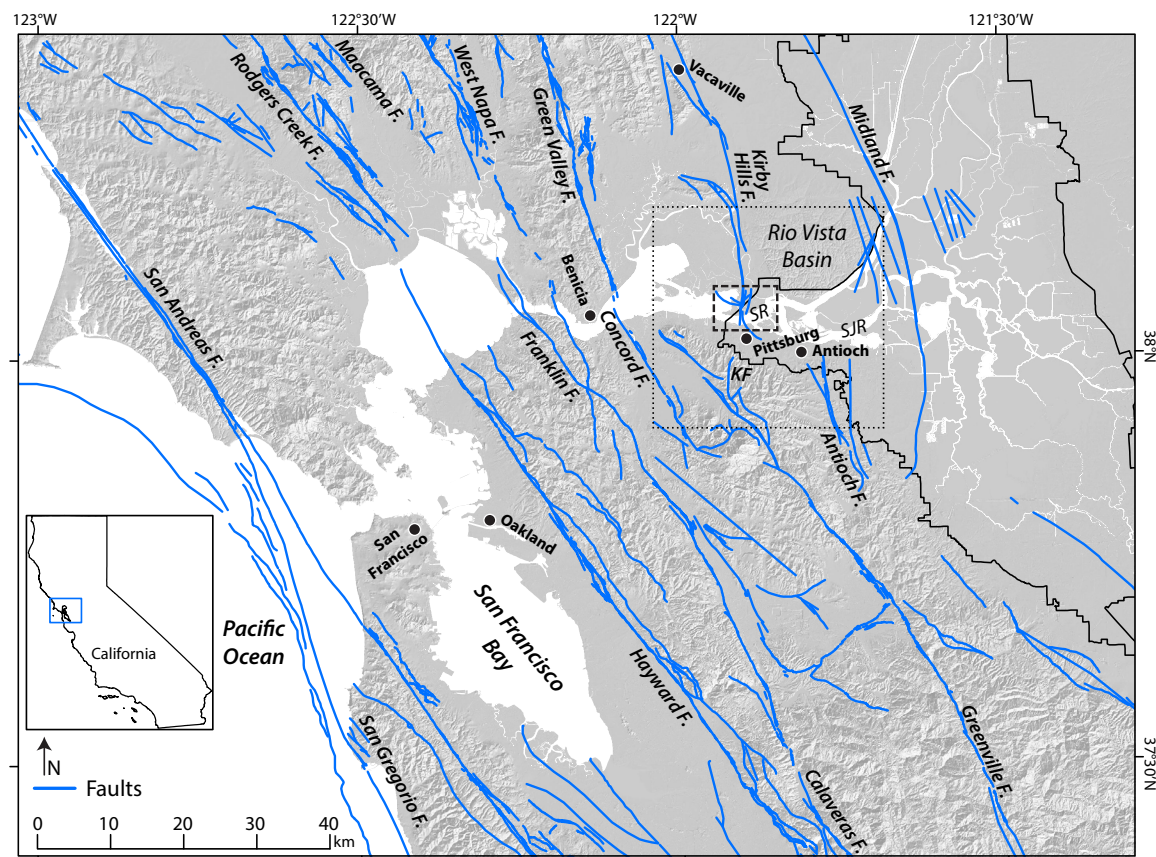
Figure 1. Map of regional Quaternary-active faults (USGS and CGS, 2020; Horton et al., 2017) and geographic landmarks, San Francisco Bay area, California (USA). Black solid outline surrounds Sacramento–San Joaquin Delta, dashed box surrounds study area, and dotted box is extent shown in Figure 3. KF—Kirker fault; SR—Sacramento River; SJR—San Joaquin River.

After the margin transitioned from subduction to mainly transform ca. 8 Ma (Atwater, 1970), the Kirby Hills fault became a strike-slip fault with an 80°–85° dip to the east (Parsons et al., 2002); it has also been defined as a reverse fault (MacKevett, 1992; Weber-Band et al., 1997). It is the easternmost part of the San Andreas fault system in this region (Fig. 1). Strike-slip displacement is estimated at 0.5 ± 0.2 mm/yr for the Kirby Hills fault (WGCEP Thrust Fault Subgroup, 1999). Vertical slip estimates are between ~0.1 and 0.5 mm/yr, but they likely fall on the lower end (~0.15 mm/yr; WGCEP Thrust Fault Subgroup, 1999).

The Kirby Hills fault is a deeply penetrating fault and is a prominent high-velocity feature, separating a shallow, low-velocity basin to the west from the gravity and velocity low of the Rio Vista Basin to the east (Thurber et al., 2009; Fletcher et al., 2016; Fletcher and Erdem, 2017). Most of the recorded seismicity (Fig. 3) on the Kirby Hills fault has occurred at depths greater than 14 km (Weber-Band et al., 1997) and as much as 25 km (Parsons et al., 2002; Thurber et al., 2009). Although most measured seismicity is below M_L 4 (Weber-Band

et al., 1997), a M 6 earthquake occurred on 19 May 1889 in the vicinity of Pittsburg and Antioch (Figs. 1 and 3; Wong et al., 1988). While the epicenter of this historical event remains ambiguous, the Kirby Hills fault is the closest known potential source for this earthquake (Weber-Band et al., 1997; WGCEP Thrust Fault Subgroup, 1999), supporting the need for continuing research on this fault.

■ METHODS

In 2017, a seismic reflection survey (Fig. 2) was conducted across the Kirby Hills fault zone in the Sacramento River using the Scripps Institution of Oceanography (La Jolla, California) Edgetech X-Star chirp subbottom profiler with line spacing between 50 and 150 m. Data were collected using a 0.7–3 kHz swept-frequency acoustic source with a 50 ms sweep and recorded in SEG-Y format with real-time GPS navigation recorded for each shot for location accuracy. The data
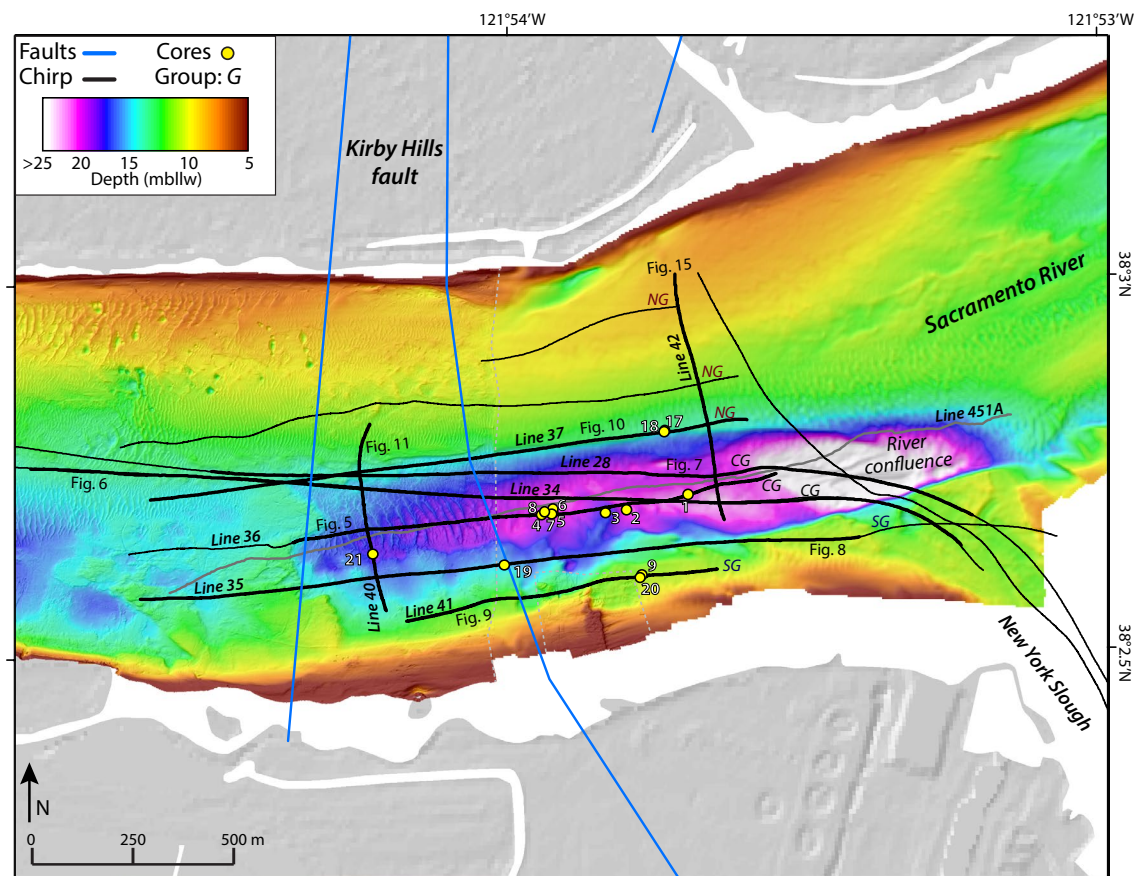
Figure 2. Map of study region where Kirby Hills fault crosses Sacramento River. Sacramento River multibeam bathymetry data relative to mean lower low water (mbllw—meters below mean lower low water) (Dasler, 2000; Pagano, 2012) are shown in colored shaded relief where available; unsurveyed waterways are shown in white. Boundaries between the two bathymetric data sets are denoted with light gray dashed line; the data sets are of differing resolutions. Faults are from USGS and CGS (2020). Chirp tracklines shown in figures are in bold, and associated figure numbers and line names are labeled. Solid gray line is air gun profile shown in Figure 6. Prefixes (DL-VC-) and leading zeroes are omitted from core labels in the figure. Map with tracklines for all data examined in this study is in Supplemental Material (see text footnote 1). NG—northern profile group; CG—central group; SG—southern group.

were processed using SIOSEIS (http://sioseis.ucsd.edu) and plotted using Seismic Unix (Cohen and Stockwell, 2015) and then imported into IHS Kingdom and QPS Fledermaus for interpretation and three-dimensional visualization. A nominal velocity of 1500 m/s was applied to convert two-way travel time (TWTT) to depth on chirp profiles. Stratigraphy was imaged as deep as 30 m below the river floor with decimeter-scale vertical resolution. Bathymetry data used in this study include National Oceanographic and Atmospheric Administration (NOAA) data set H12340 (Pagano, 2012) with 1 m resolution and NOAA data set H10897 (Dasler, 2000) with 5 m resolution, with a vertical scale relative to mean lower low water.

Seismic reflection data collected and processed by the U.S. Geological Survey (USGS) in the 1990s were also utilized (Supplemental Material[2]; Childs et al., 2000).

This includes low-frequency Bolt 600 air gun data (surveys J2-94-SF and G2-95-SF) and higher-frequency Seistec boomer data (survey J2-94-SF). The data were imported into IHS Kingdom to aid in interpretation of fault-related deformation.

In 2018, vibracores were collected at the study site from the S/V *Retriever* (Fig. 2). The cores were collected using the USGS Rossfelder P-5 vibracoring system. Locations for cores used in this study are listed in Table 1. Core names have a prefix of DL-VC-, which stands for delta-vibracore, but cores will be referred to by the core number without prefix in the following sections. Due to the density of the material, penetration was quite poor in many coring locations. As a result, these sediments ended up in ordered bags instead of core liners. These cores are noted in Table 1. Whole cores were analyzed using a Geotek
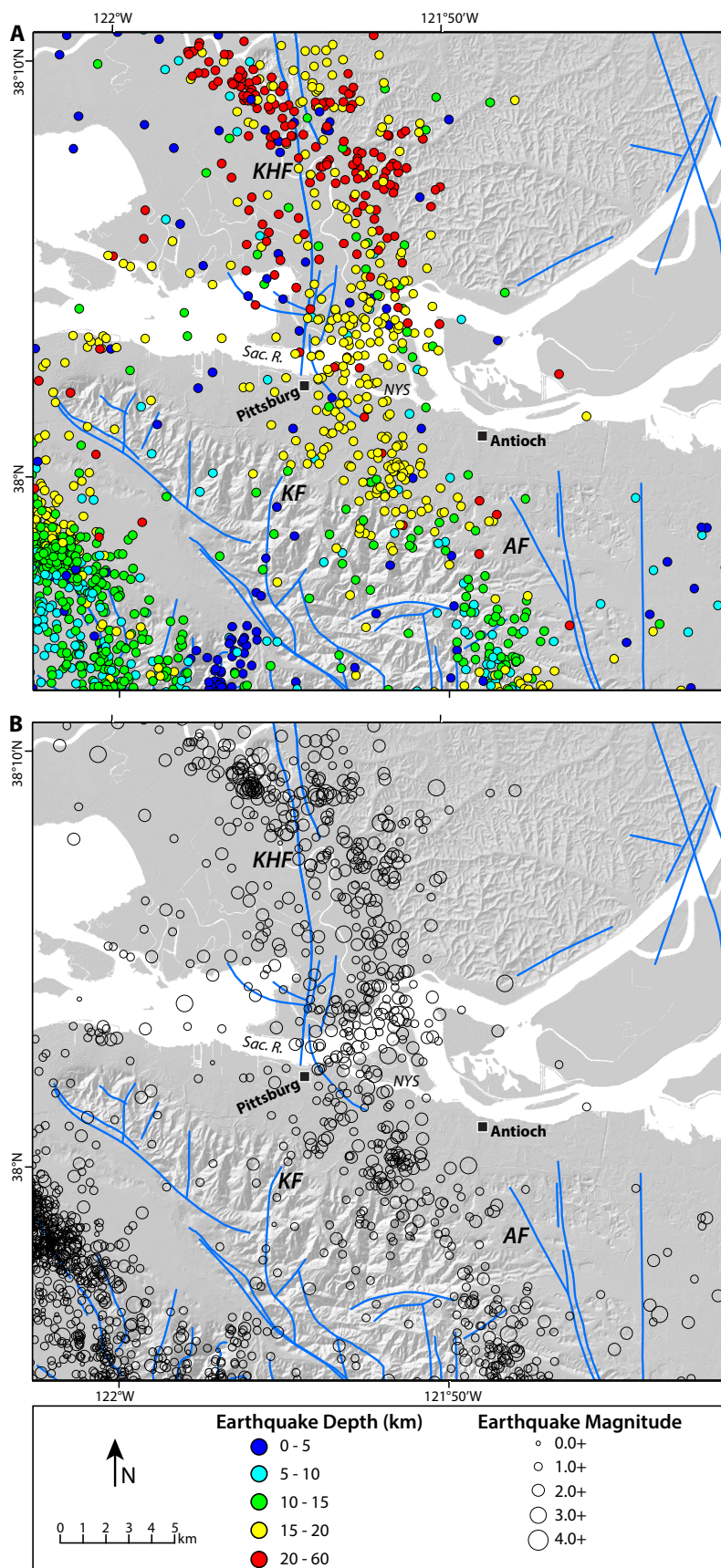
Figure 3. Seismicity data since 1969 CE (Northern California Earthquake Data Center, 2014) with faults plotted as blue lines (USGS and CGS, 2020; Horton et al., 2017). (A) Earthquake depth in kilometers. (B) Earthquake magnitude. KHF—Kirby Hills fault; KF—Kirker fault; AF—Antioch fault; Sac. R.—Sacramento River; NYS—New York Slough.

TABLE 1. INFORMATION ABOUT SEDIMENT CORES USED IN THIS STUDY

Core name	Latitude (°N)	Longitude (°W)	Water depth (m)	Length (cm)
DL-VC-01	38.04518	121.89505	20.7264	100
DL-VC-02	38.04486	121.8968	20.78736	1 bag
DL-VC-03	38.04479	121.8974	18.77568	1 bag
DL-VC-04	38.04476	121.8992	21.09216	53.5
DL-VC-05	38.0448	121.89887	22.37232	21
DL-VC-06	38.04489	121.89888	22.58568	4 bags
DL-VC-07	38.04478	121.89892	22.58568	1 bag
DL-VC-08	38.04483	121.89911	22.00656	1 bag
DL-VC-09	38.0434	121.89639	12.89304	1 bag
DL-VC-17	38.04662	121.89568	16.97736	29
DL-VC-18	38.04659	121.89571	17.9832	1 bag
DL-VC-19	38.04365	121.90027	16.48968	4 bags
DL-VC-20	38.04333	121.89643	12.58824	51
DL-VC-21	38.04393	121.90398	19.78152	42

Notes: If there was no intact sample recovered in a core tube, any recovered material was stored in bags.

multi-sensor core logger for downcore measurement of physical properties. Organic samples were analyzed at the W.M. Keck Carbon Cycle Accelerator Mass Spectrometer Facility at University of California Irvine. The radiocarbon ages (Table 2) were calibrated and converted to calendar chronology using OxCal version 4.4 (Bronk Ramsey, 2009), with calibration curve IntCal20 (Reimer et al., 2020), which includes Bomb series data from the Bomb13NH2 calibration curve (Hua et al., 2013). One date with a reported ^{14}C result of "modern" was converted to calendar age using CALIBomb (Reimer and Reimer, 2022; http://calib.org/CALIBomb/). Except for the "modern" date, calendar chronology for all samples in the text and figures is in yr B.P., meaning years prior to 1950 CE, but years BCE or CE are also listed in Table 2.

■ RESULTS

River Floor Morphology

The Kirby Hills fault crosses the Sacramento River at a bend in the channel and near the confluence of the river with New York Slough (Figs. 1–4). There is a large bathymetric low (as much as ~30 m deep on the eastern end) at the

## TABLE 2. RADIOCARBON ACCELERATOR MASS SPECTROMETER DATES FROM SEDIMENT CORES

Lab no.*	Core	Sample depth (cm)	Material	Fraction modern[†]	δ^{14}C[†] (‰)	Reported ^{14}C age[†] (yr B.P.)	Calibrated ages (yr B.P.)			Calibrated ages (BCE/CE)			Unit
							From	To	%	From	To	%	
212878	DL-VC-04	15–17	Shells	1.0249 ± 0.0017	24.9 ± 1.7	Modern[§] ± N/A	–	–	–	1956.05[§]	1956.54[§]	95	1
212879	DL-VC-04	30–32	Shells	0.9841 ± 0.0017	−15.9 ± 1.7	130 ± 15	268	14	95.4	1682	1937	95.4	1
212907	DL-VC-04	36–37	Seed cap	0.7837 ± 0.0017	−216.3 ± 1.7	1960 ± 20	1942	1827	95.4	8	123	95.4	1
212885	DL-VC-04	36–37	Wood fragments	0.7979 ± 0.0013	−202.1 ± 1.3	1815 ± 15	1743	1633	95.4	208	317	95.4	1
212886	DL-VC-04	40–42	Wood fragments	0.6157 ± 0.0010	−384.3 ± 1.0	3895 ± 15	4412	4250	95.4	−2463	−2301	95.4	3
212906	DL-VC-05	8–10	Wood fragments	0.8103 ± 0.0012	−189.7 ± 1.2	1690 ± 15	1689	1536	95.4	262	415	95.4	1
212904	DL-VC-17	9–11	Wood fragments	0.6926 ± 0.0011	−307.4 ± 1.1	2950 ± 15	3173	3005	95.4	−1224	−1056	95.4	1
212905	DL-VC-17	9–11	Charcoal	0.6575 ± 0.0011	−342.5 ± 1.1	3370 ± 15	3685	3565	95.4	−1736	−1616	95.4	1
212883	DL-VC-20	4–5	Shell	0.9838 ± 0.0015	−16.2 ± 1.5	130 ± 15	268	14	95.4	1682	1937	95.4	3
212887	DL-VC-21	7–8	Peat	0.8847 ± 0.0014	−115.3 ± 1.4	985 ± 15	930	799	95.4	1021	1152	95.4	1
212888	DL-VC-21	7–8	Peat	0.8653 ± 0.0014	−134.7 ± 1.4	1160 ± 15	1178	993	95.4	772	957	95.4	1
212909	DL-VC-21	21–22	Peat	0.5566 ± 0.0010	−443.4 ± 1.0	4705 ± 15	5477	5325	95.4	−3528	−3376	95.4	1
212889	DL-VC-21	30–32	Peat	0.4963 ± 0.0009	−503.7 ± 0.9	5630 ± 15	6482	6317	95.4	−4533	−4368	95.4	1
212890	DL-VC-21	30–32	Peat	0.4962 ± 0.0009	−503.8 ± 0.9	5630 ± 15	6482	6317	95.4	−4533	−4368	95.4	1

Notes: Sample preparation backgrounds have been subtracted, based on measurements of ^{14}C-free wood. N/A—not available. Dashes in calibrated ages column indicate no value. Calibration information is in the Methods section (see text). %—percent confidence interval for oxcal output. Negative years are BCE; this is the calibration output from oxcal for BCE/CE. Unit—interpreted sediment unit.
   *University of California Irvine W.M. Keck Carbon Cycle Accelerator Mass Spectrometer Facility.
   [†]Radiocarbon concentrations are given as fractions of the modern standard, δ^{14}C, and conventional radiocarbon age, following the conventions of Stuiver and Polach (1977). All results have been corrected for isotopic fractionation according to the conventions of Stuiver and Polach (1977), with δ^{13}C values measured on prepared graphite using the accelerator mass spectrometer.
   [§]Modern date was converted to calendar age using CALIBomb (Reimer and Reimer, 2022; http://calib.org/CALIBomb/).
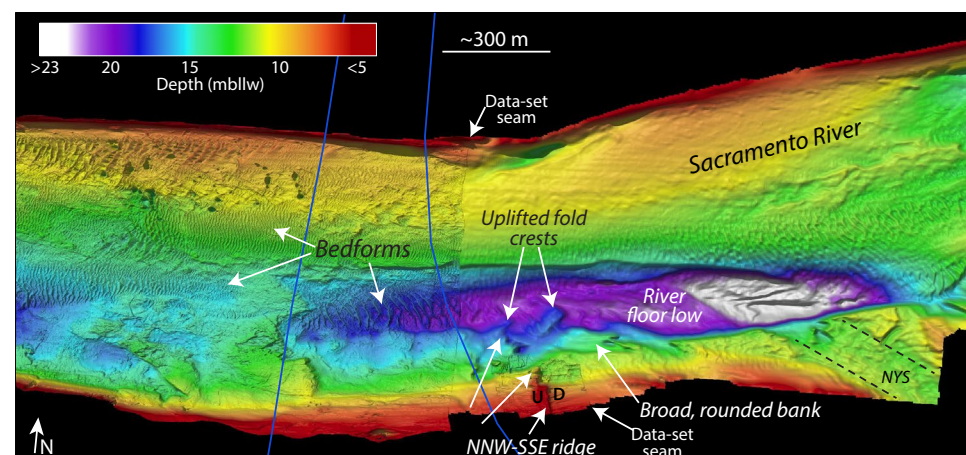
Figure 4. High-resolution bathymetry vertically exaggerated 6× relative to the horizontal distance (Dasler, 2000; Pagano, 2012) with features labeled. Bathymetric data set view and extent are similar to what is shown in Figure 2. The two bathymetric data sets are merged, but of different resolutions. Depth is in meters below mean lower low water (mbllw). Kirby Hills fault is denoted by blue lines (USGS and CGS, 2020). Dashed black lines denote edges of shipping channel. U—up; D—down; NYS—New York Slough.

southern side of the bend, where the river floor is deformed by the Kirby Hills fault (Fig. 4). Here, there are two mounds in the shape of large-scale linguloid bedforms in the bathymetric data. However, these features are not true fluvial bedforms; they are the crests of folded strata (Fig. 4), confirmed by the chirp data discussed in the next section. The larger of the two is ~150 m from side to side, ~150 m in length from trough to trough, and ~2.5 m in height. The actual fluvial bedforms in the river floor low are more sinuous to catenary with wavelengths between 15 and 25 m and heights up to 1.5 m. Outside of the bathymetric low, bedforms are also sinuous to catenary with wavelengths typically less than 10 m and heights less than 0.5 m. A broad, rounded bank extends into the river floor low from the south and is associated with the Kirby Hills fault (Fig. 4). There is also a distinct NNW-SSE–trending bathymetric high extending from the southern shoreline. This feature is characterized by a sharp east-facing scarp (Fig. 4).

Acoustic Features, Units, and Surfaces in Chirp Data

The close spacing of the new subbottom data (~100 m; Fig. 2) allows us to document the lateral changes in acoustic character along this ~600 m section of the Kirby Hills fault zone in high resolution. On the basis of acoustic character, the profiles can be divided into three groups associated with the location of the profiles within the river channel (Fig. 2): southern, central (within the low), and northern. Our data do not image any surface rupture or fault planes but do document folding and deformation related to faulting at depth.

The Kirby Hills fault zone is characterized by a monocline with west-dipping strata (Figs. 5–9) in the top ~30 m of the subsurface in chirp data. Folding is evident in air gun data down to at least 0.6 s TWTT (Fig. 6B; ~0.6 km; Parsons et al., 2002), but deformation associated with the fault extends to ~3 s TWTT

in lower frequency multi-channel seismic data (~6–9 km; Parsons et al., 2002). The monocline breaches the river floor, making up the large mounds traversed by the central group of chirp profiles (Figs. 2, 4, and 5–7). The eastern side of the monocline forms the broad, rounded bank observed in the river floor low, and small highs on the fold make up the NNW-SSE ridge; both features are traversed by the southern-group profiles (Figs. 2, 4, 8, and 9). The fold is buried north of line 34 (Figs. 2, 7, and 10).

There are four acoustic units and two main unconformities identified in the chirp data in the vicinity of the Kirby Hills fault zone. The acoustic units were defined based on their acoustic character, stratigraphic relationship to the other units, and bounding unconformities. The acoustic units and unconformities are numbered from youngest to oldest starting at 1.

Acoustic unit 4 is the oldest unit and is defined by low- to high-amplitude, relatively parallel reflectors, which are warped where the unit is folded, forming the monocline in the Kirby Hills fault zone (Figs. 5–9). Unit 4 also forms the majority of the broad, rounded bank and part of the NNW-SSE ridge (Figs. 4, 8, and 9). The acoustic character of this unit is different on either side of the monocline. On the western side, reflectors gently dip westward away from the fold at ~5°–6° (Figs. 5–9), gradually flattening out to the west (Figs. 11 and 12), and have relatively high acoustic amplitude. On the eastern side of the fold in unit 4 are westward-dipping reflectors that have low acoustic amplitude and dip at ~5°–10° (Parsons et al., 2002) in the central group but have high acoustic amplitude and dip at ~4° in the southern group (Figs. 8 and 9). The uppermost acoustic packages within unit 4 in both air gun (Parsons et al., 2002) and chirp data thin onto the fold from west to east, suggesting folding during deposition (Figs. 5–8). Acoustic unit 4 and the monocline are not imaged in the northern group of profiles (Fig. 2); gas wipes out the stratigraphy in the two northernmost profiles, and in the other profile (Fig. 10), unit 4 is deep enough that it is obscured by the water bottom multiple reflection.
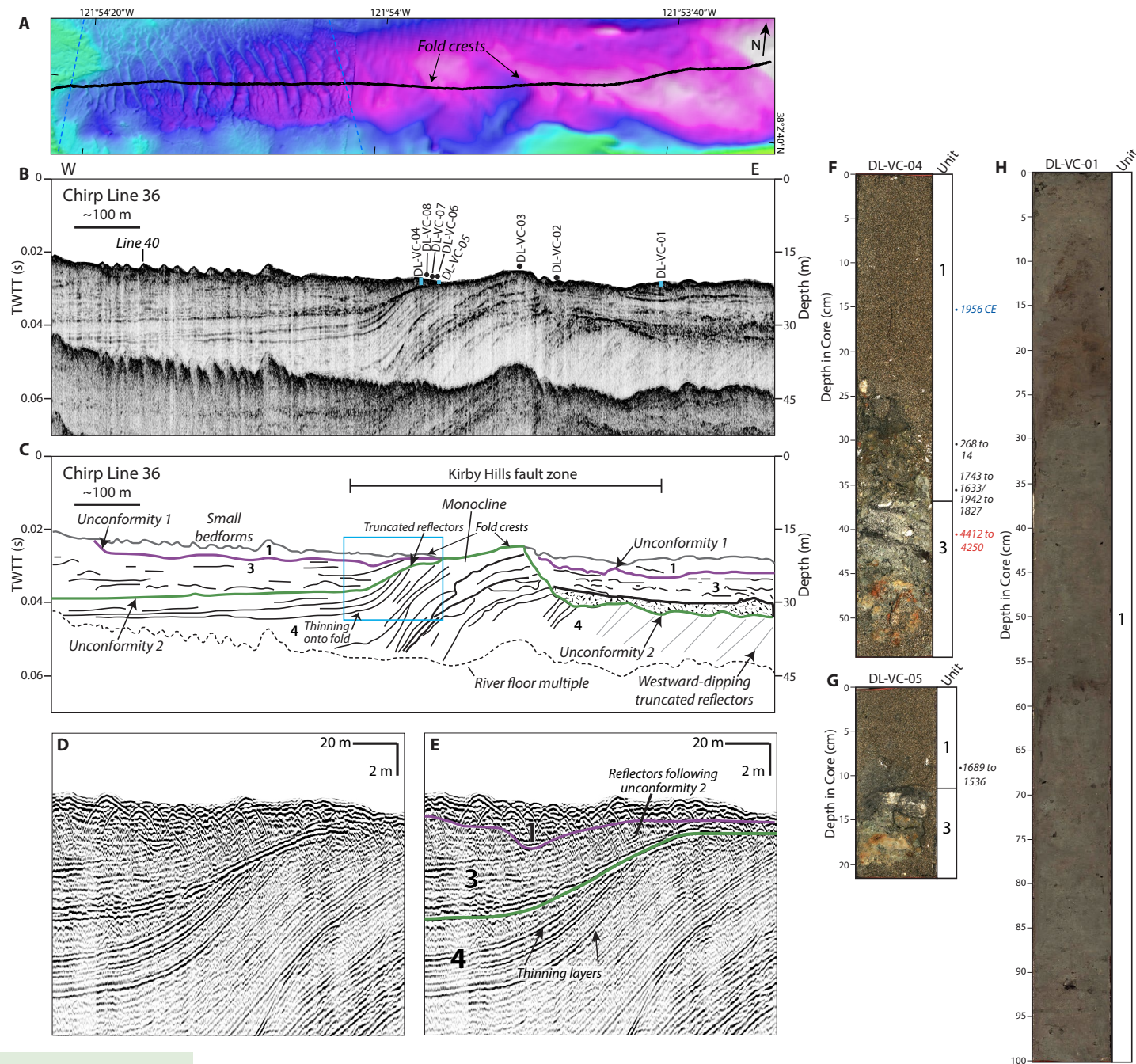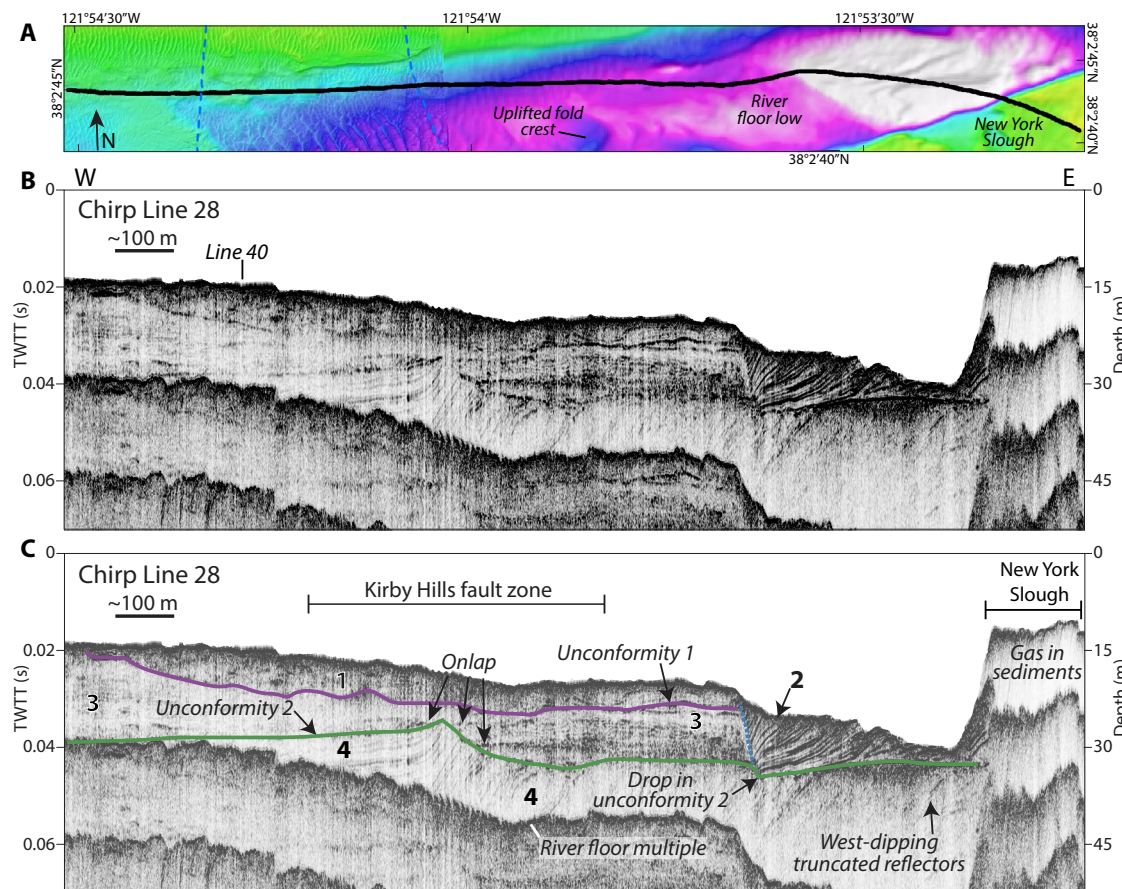
Figure 5. (A–E) Section of central group chirp profile 36 with trackline over bathymetry (A), uninterpreted profile (B), and interpretations showing numbered acoustic units and unconformities (C); zoomed in section of western side of monocline (blue box in C) is shown uninterpreted (D) and interpreted (E). Unconformity 1 is obscured near the west side of the monocline due to sound diffractions from the river floor. Chirp trackline is shown in black and faults are blue dashed lines in A. For additional bathymetry context, see Figure 2. Core locations are shown in B; where there was penetration, core depths are drawn approximately to scale (blue bars). TWTT—two-way travel time. (F–H) Interpreted units and calibrated radiocarbon dates are shown next to images of core DL-VC-04 (F), core DL-VC-05 (G), and core DL-VC-01 (H). Dates are red where inferred to be mixed in by a younger process that disturbed sediments. All dates are in yr B.P. except the modern date (in blue), which is in years CE. Note, sand at bottom of cores in F and G is an artifact of the coring process and not representative of unit 3.
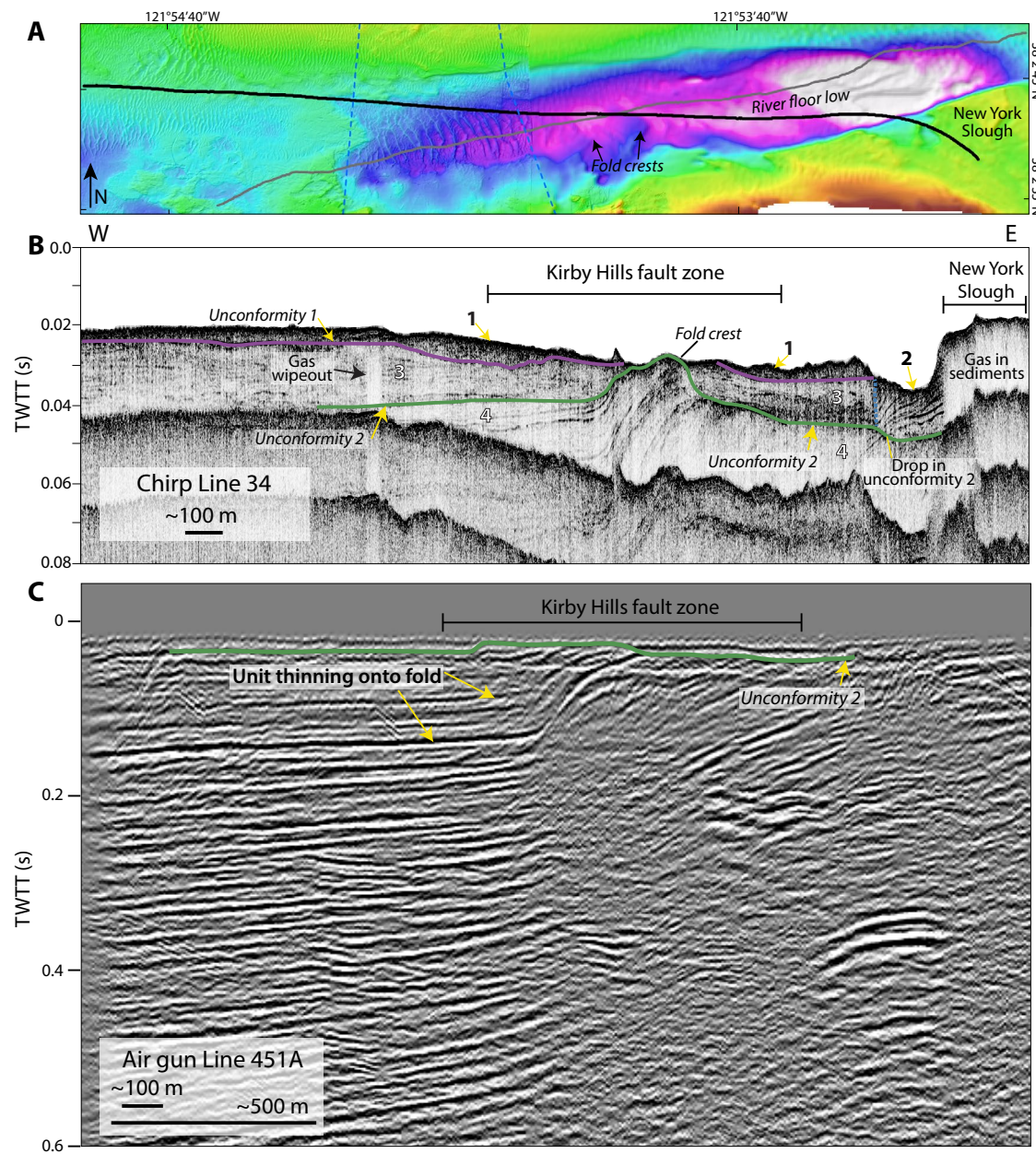
Figure 6. Trackline over bathymetry (A) for comparison between a section of central group chirp profile 34 with interpretations showing numbered acoustic units and unconformities (B) and a section of U.S. Geological Survey air gun profile 451A with interpretations (C). Chirp trackline is shown in black, air gun trackline is shown in gray, and faults are blue dashed lines in A. For additional bathymetry context, see Figure 2. Two-way travel time (TWTT) in B represents approximately same distance as the same time in uppermost portion of C. Portion of line 34 that crosses into New York Slough is marked. Dashed blue line in B is local unconformity between units 2 and 3.
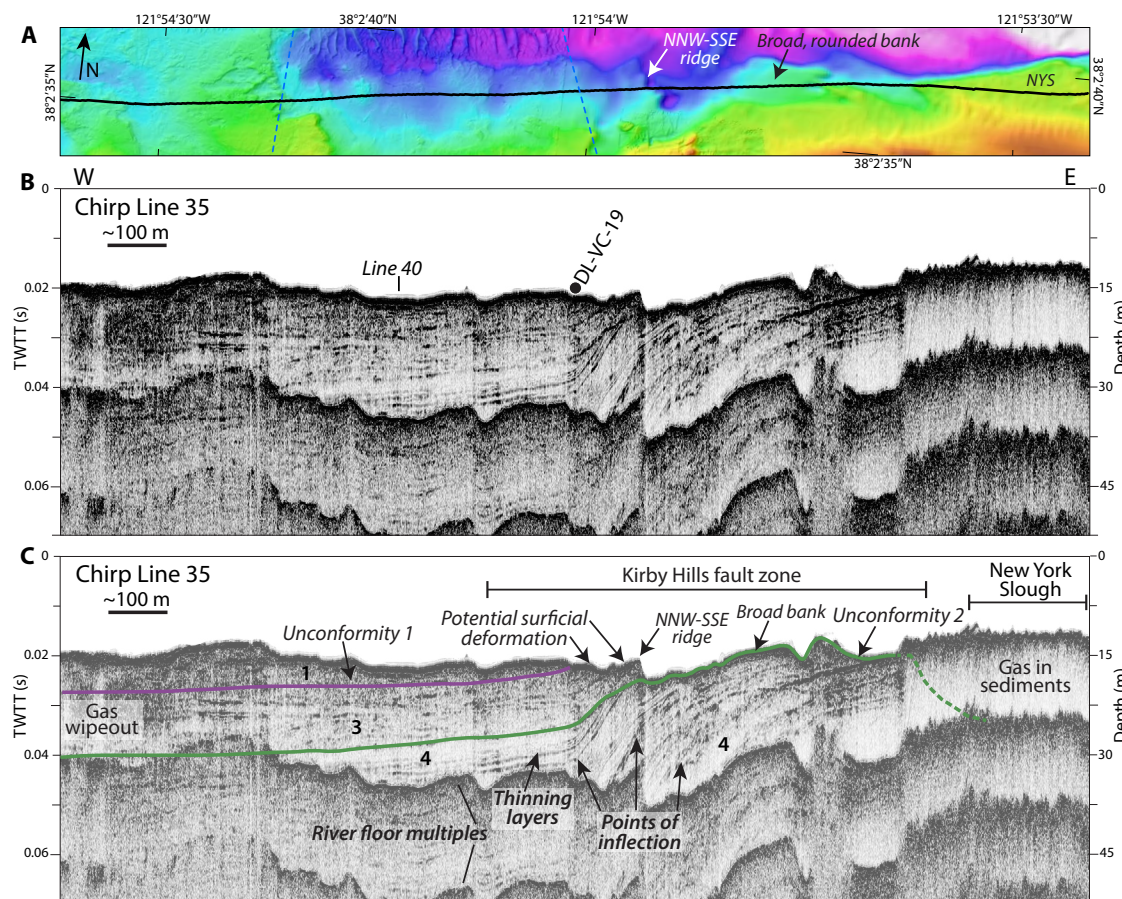
Figure 7. Section of central group chirp profile 28 with trackline over bathymetry (A), uninterpreted profile (B), and interpreted profile showing numbered acoustic units and unconformities (C). Chirp trackline is shown in black and faults are blue dashed lines in A. For additional bathymetry context, see Figure 2. Dashed blue line in C is local unconformity between units 2 and 3. TWTT—two-way travel time.

At the monocline in the central and southern groups, the internal reflectors of unit 4 dip at varying angles because they have been uplifted and deformed (Figs. 5–9). Where there are changes in reflector dip angle associated with the fold, the points of inflection were mapped (Fig. 13A). There are three inflection points that generally diverge from north to south across the river channel. This is the same trend as the zone of deformation associated with the Kirby Hills fault. In the southern group, the zone of deformation is broadest, between 300 and 500 m wide along the river channel (Figs. 8 and 9). There is also some gas wipeout at the fold (Fig. 9). In the central group, the zone of deformation is ~200–300 m wide along the channel (Figs. 5–7). The monocline in the northernmost profile in this group (line 28; Fig. 7) has a different character than in the other profiles (Fig. 12), likely due to variable erosion within an active river channel. Differences could also be due to a change in strike of the feature relative to the chirp profile.

The dipping reflectors of acoustic unit 4 are truncated by an unconformity that extends to the east and west of the fold, defined as unconformity 2 (Figs. 5–12). Unconformity 2 is exposed at the river floor at the monocline and to the east in the southern group (Figs. 5, 6, 8, and 9). In the northern group, unconformity 2 is broadly uneven, with more than 8 m of depth variation across profile 37 (Fig. 10). This pattern could be the result of fluvial incision and/or fault activity. The river floor multiple partially obscures unconformity 2 here, but its depth is confirmed via crossing lines.

A gridded depth-to-surface map of unconformity 2 (Fig. 13B) was computed with flex gridding and a 60 m radius, based on interpretation of the unconformity on the chirp profiles. The surface (Fig. 13B) shallows near mapped traces of the Kirby Hills fault and fault-related features, such as the uplifted fold crests (~21 m below water level; mbwl), with the shallowest portion of the surface in the southern part of the river channel (~10 mbwl) where there
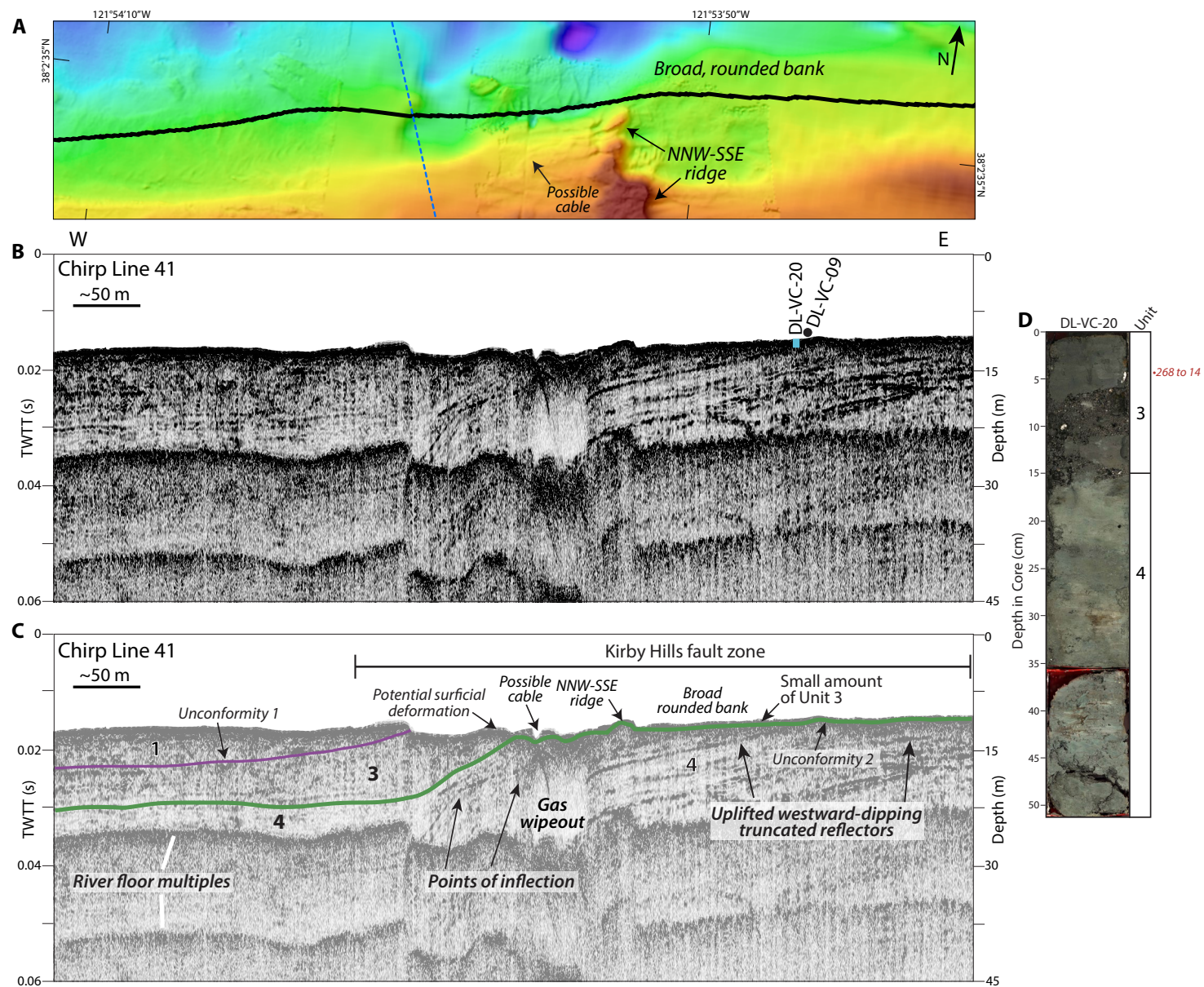
Figure 8. Southern group chirp profile 35 with trackline over bathymetry (A), uninterpreted profile (B), and interpreted profile showing numbered acoustic units and unconformities (C). Chirp trackline is shown in black and faults are blue dashed lines in A. For additional bathymetry context, see Figure 2. Unconformity 2 is a solid line where mapped and dashed where it is obscured by gas, but the location is based on correlation to other profiles. NYS—New York Slough; TWTT—two-way travel time.

is more apparent uplift. The surface deepens to the northwest (dropping to ~26–27 mbwl) and toward the north-northeast (dropping to ~43 mbwl, but mostly 32–34 mbwl). To rule out differential erosion as the sole cause of the uneven unconformity 2 surface, a specific stratigraphic feature in the chirp data was identified and mapped to identify its change in depth (see Supplemental Material [see footnote 1] for more details). No change in depth or a lack of discernible trend would indicate the unconformity 2 surface was variable solely due to differential erosion, while a similar trend to the surface supports some tectonic influence. The feature that was mapped was where a layer pinches out on the western side and/or center of the monocline and the reflectors above and below it dip at different angles. This pinch-out feature does not have the same exact expression across the chirp profiles, but it was the best option for these data because there is no clear fold axis. This feature was discernible

in the southern and central profiles but was too deep to be resolved in the northern profiles. The pinch-out feature deepens from the south to the north across the river channel, going from ~22 mbwl to ~35 mbwl over 335 m of distance. Although the depths picked could be slightly off, the overall southward shallowing trend is the same trend as that of unconformity 2, which supports the tectonic influence on the depth of unconformity 2 (Fig. 13B).

Acoustic unit 3 is located directly above unconformity 2 on both sides of the monocline as well as above the fold where the unconformity is not exposed at the river floor (Figs. 5–12). Unit 3 is primarily defined by discontinuous, flat-lying reflectors of varying acoustic amplitude. In the southern profile group, unit 3 thins onto the fold from the western side (Fig. 8). On the eastern side, there is no mapped unit 3, but there is a small amount present in the southernmost line (Fig. 9) based on sediment cores (described in the
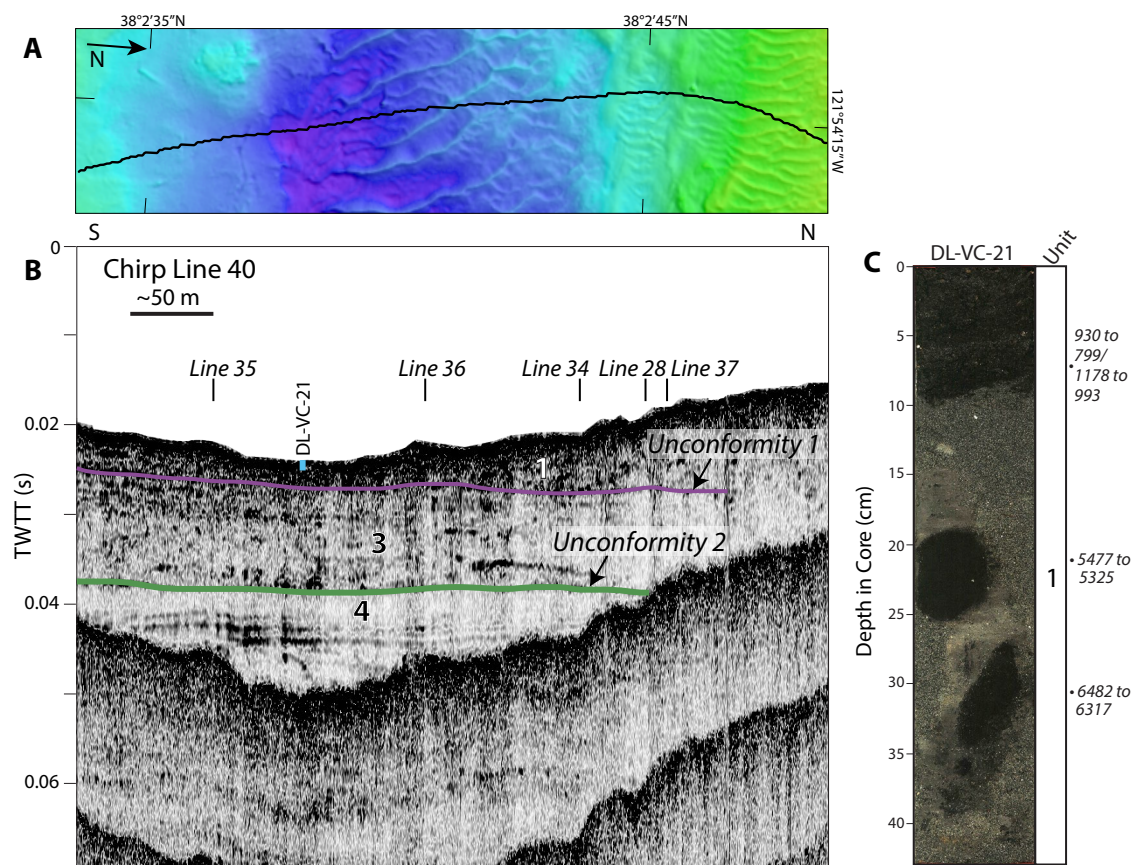
Figure 9. (A–C) Southern group chirp profile 41 with trackline over bathymetry (A), uninterpreted profile (B), and interpreted profile showing numbered acoustic units and unconformities (C). Chirp trackline is shown in black and fault is blue dashed line in A. For additional bathymetry context, see Figure 2. Core locations are shown in B; where there was penetration, core depth is drawn approximately to scale (blue bar). (D) Image of core DL-VC-20, interpreted units, and calibrated radiocarbon date in yr B.P. Date is shown in red, denoting contamination of unit by a younger process, likely the edge of the core tube pushing the shell down from the surface. TWTT—two-way travel time.
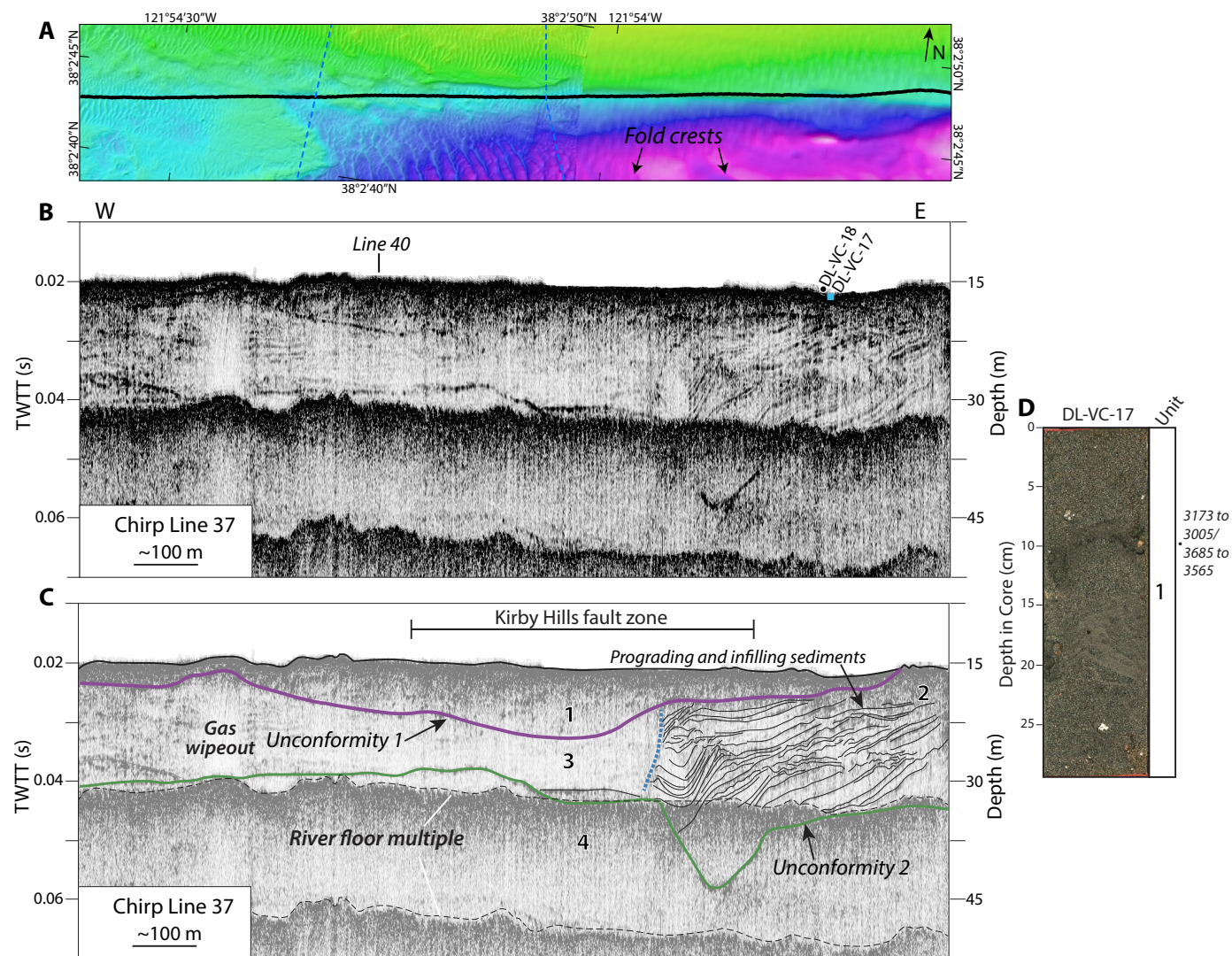
Figure 10. (A–C) Northern group chirp profile 37 with trackline over bathymetry (A), uninterpreted profile (B), and interpreted profile showing numbered acoustic units and unconformities (C). Chirp trackline is shown in black and faults are blue dashed lines in A. For additional bathymetry context, see Figure 2. Dashed blue line in C is local unconformity between units 2 and 3. Core locations are shown in B; where there was penetration, core depth is drawn approximately to scale (blue bar). TWTT—two-way travel time. (D) Image of core DL-VC-17, interpreted unit, and calibrated radiocarbon dates in yr B.P.

Figure 11. (A–B) Cross-channel chirp profile 40 with trackline over bathymetry (A) and interpreted version of profile showing numbered acoustic units and unconformities (B). Core depth is shown approximately to scale (blue bar). TWTT—two-way travel time. (C) Image of core DL-VC-21, interpreted unit, and calibrated radiocarbon dates in yr B.P.

next section). This is difficult to observe in chirp data due to the limits of vertical resolution. In the central profile group, the lower portion of unit 3 on the western side of the fold follows the shape of unconformity 2 and in some places onlaps it (Figs. 5–7). On the eastern side of the fold, internal reflectors within unit 3 gently dip eastward away from the fold, except directly east of the most uplifted portion of the fold, where the unit is more acoustically chaotic. In line 28 (Fig. 7), the reflectors within unit 3 appear to onlap unconformity 2 on both sides of the fold. In the northern profile group, there is no imaged fold, but unit 3 sediments blanket unconformity 2 (Fig. 10). Based on stratigraphic correlation with the rest of the data, unit 3 is present on the western side of the profile, where it has low-amplitude, flat-lying internal reflectors (Fig. 10).

Within the deepest part of the river floor low (~22 mbwl and below) and just to the north of it, near the confluence of the Sacramento River and New York Slough, is an acoustic unit with high-amplitude northwestward-dipping reflectors, defined as acoustic unit 2 (Figs. 2, 6–7, 10, and 12). This unit lies above unconformity 2 and downlaps onto it. Unit 2 also abuts unit 3 and is separated from it by a local unconformity with an eastern dip (~20°–40°). The reflectors in unit 2 form a progradational pattern, filling in lows in unconformity 2 (Figs. 6–7 and 10). The reflectors increase in steepness from the base of the unit to the river floor (from ~1° to >10°) because unit 2 is blocked to the west by unit 3. Unit 2 is between 6 and 9 m thick where it is present in the river floor low (Figs. 6–7), but the unit is between 8 and 20 m thick north of the low in the northern chirp group where it appears on the eastern side of line 37 (Fig. 10). There, unit 2 has multiple sets of westward-dipping reflectors of medium amplitude, interpreted as stacked sets of prograding sediments. Where unconformity 2 climbs upward by ~8 m, the overlying reflectors in unit 2 are curved concave up, with disturbance on the eastern side (Fig. 10).
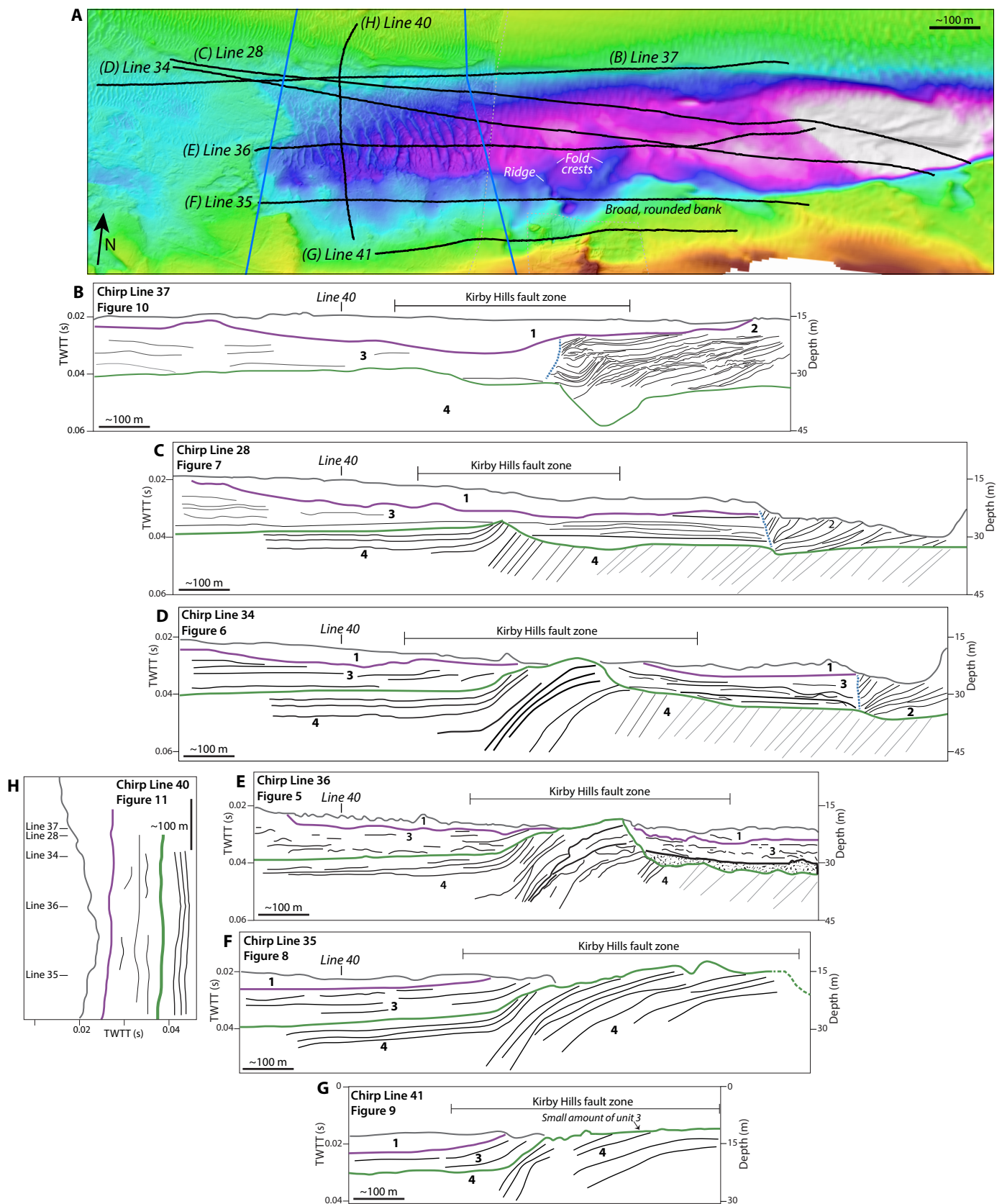
Figure 12. Compilation of stratigraphic evolution across study area. (A) Map with tracklines of shown chirp profiles in black, faults in blue, and bathymetric data set seam as gray dashed line. For additional bathymetry context, see Figure 2. (B–G) Interpretations of west-east–trending chirp profiles, ordered from north to south, approximately scaled and positioned to tracklines in map in A. Acoustic units are numbered 1 to 4. (H) Interpretation of north-south chirp profile 40 is shown along the west-east profiles at the same scale. Unconformity 1 is in purple and unconformity 2 is in green. TWTT—two-way travel time.

Figure 13. (A) Monocline points of inflection (large arrows) plotted on bathymetry data (Dasler, 2000; Pagano, 2012). Plunge and dip directions shown. Mapped gas areas near western strand of Kirby Hills fault are also shown (black areas). Bathymetry is in meters below mean lower low water (mbllw). (B) Depth to surface map of unconformity 2 in meters below water level (mbwl). Black lines are 5 m contours. Fault traces are from USGS and CGS (2020).


Units 2 and 3 are in places truncated by an erosional unconformity, defined as unconformity 1 (Figs. 5–12). Where present on the western side of the monocline, unconformity 1 commonly dips toward the east, deepening from ~1 to ~8 m below the river floor (Figs. 6–7 and 10). On the eastern side of the fold, unconformity 1 is flatter but with some small-scale undulation and lies as much as 5 m below the river floor (Figs. 5–7 and 10).

Above unconformity 1, overlying units 3 and 2, is acoustic unit 1. This unit has no well-defined internal stratigraphy but contains some short, high-amplitude reflectors and other discontinuous reflectors of varying amplitude (Figs. 5–12). Unit 1 is less than 10 m in thickness but generally less than 5 m thick in the study area. In the southern profile group, unit 1 has some reflectors that have the same trend as unconformity 1, suggesting potential uplift post-deposition (Figs. 8 and 9). Overall, unit 1 is the dominant unit exposed at the river floor (Fig. 14). Unit 2 is exposed on the eastern side of the study area, while units 3 and 4 are variably exposed near the monocline (Fig. 14).

Sediment Cores

Vibracore penetration and recovery was poor because of the various lithologies encountered along the Kirby Hills fault zone. Only 6 of the 14 vibracore attempts (Figs. 2, 5, and 9–11; Table 1) in the study area were successful in collecting a sequence of sediments in the core liner. Material recovered from other attempts was either too coarse and unconsolidated (pebbles, cobbles, sticks) or too dense (clay) to be retrieved as whole cores and was retained in large sample bags. Material from the core catcher and cutter from successful cores was also retained in sample bags. The cores sampled acoustic units 1, 3, and 4, and the sedimentary units are defined with the same numbers. None of the cores sampled unit 2.

The sediments of unit 1 vary throughout the study area (cores 01, 04, 05, 17, and 21; Figs. 2, 5, and 10–11), including within the river floor low (Figs. 2 and 5). Unit 1 sediments in cores 04 and 05 (Figs. 2 and 5), on the western side of the monocline, are dark brownish gray sands. On the eastern side of the fold in core 01 (Figs. 2 and 5), unit 1 sediments are a clay–fine sand mixture that is dark gray mottled with medium brown. North of the river floor low, in core 17 (Figs. 2 and 10), unit 1 is primarily dark grayish brown medium sand with some isolated clay layers. West of the river low, in core 21 (Figs. 2 and 11), unit 1 is composed of sands that are primarily greenish black as well as peat and other organic layers.
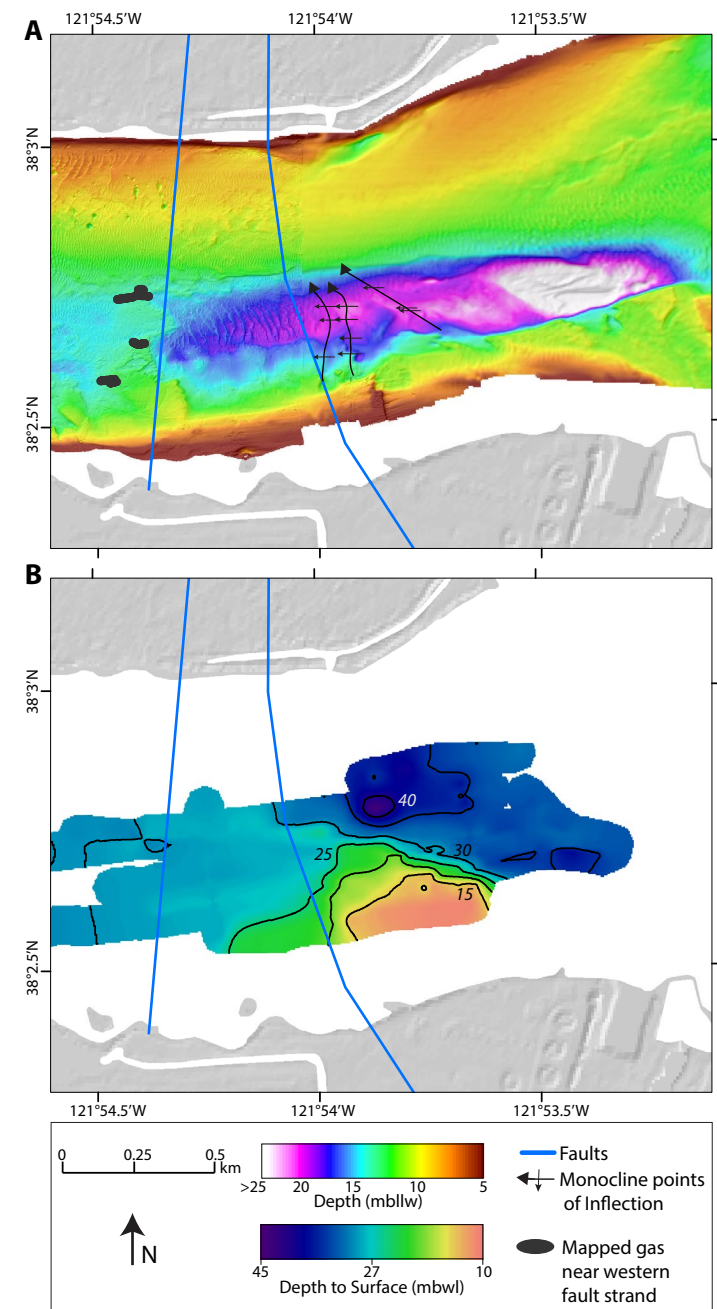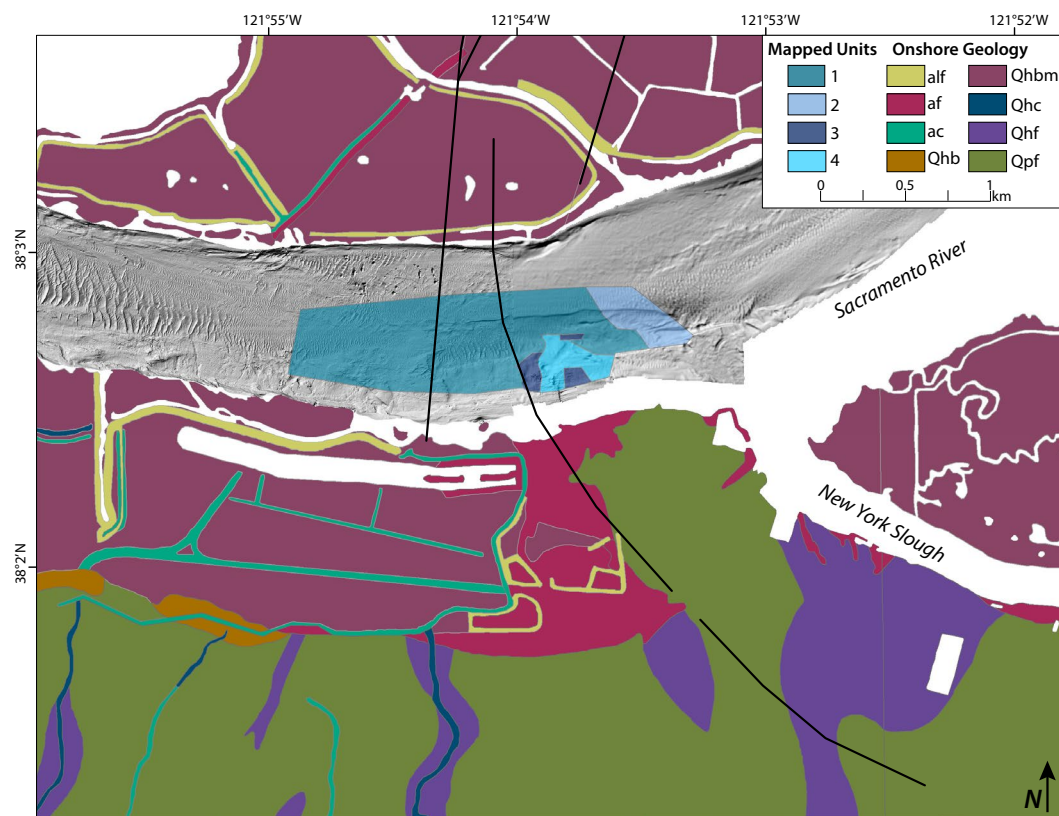
Figure 14. Map of geologic interpretations of surficial units 1 to 4 based on chirp data, overlain on shaded-relief bathymetry (Dasler, 2000; Pagano, 2012). Unsurveyed water bottom is shown in white. Fault traces are black solid lines and are from USGS and CGS (2020). Onshore geologic units are from Graymer et al. (2002). alf—artificial levee fill (historical); af—artificial fill (historical); ac—artificial channel deposits (historical); Qhb—basin deposits (Holocene); Qhbm—bay mud deposits (Holocene); Qhc—stream channel deposits (Holocene); Qhf—alluvial fan deposits (Holocene); Qpf—alluvial fan deposits (late Pleistocene).

Unit 3 (cores 04, 05, 19, and 20; Figs. 2, 5, 8, and 9) is composed primarily of dark greenish gray clay and fine to coarse sand mixed with rocks (typically <2 cm in diameter). On the monocline within the river floor low (cores 04 and 05; Figs. 2 and 5), unit 3 also has large oxidized (rusty) patches. These cores also have sand at the bottom, but this was an artifact of the coring process because some unconsolidated sands from the top of the core were able to flow down the sides of the core tube where there were gaps in consolidated unit 3. Other material collected from above unconformity 2 at the monocline in the river floor low, where there was little to no penetration, ranged from unconsolidated medium sands to mixed rocks (typically less than 5 cm in diameter), cobbles, sticks, and shells.

Unit 4 was captured by cores 09 and 20 and the core cutter sample of core 05 (Figs. 2 and 9). The sediments are primarily dense clay ranging from greenish gray to dark greenish gray to dark grayish brown. Some fine sand and pebbles are present in core 05 and shells in core 09, but this is likely because the sample was from the river floor. Preliminary analysis of units 4 and 3 from cores 04, 05, 09, 19, and 20 by X-ray diffraction (Young, 2019) indicated variability in the clay composition between the units. Unit 4 has chlorite, whereas none was detected in unit 3.

Radiocarbon dates from unit 1 indicate an age of Holocene to modern (post–1950 CE) for the unit. Dates from unit 1 in the river floor low (Figs. 2 and 5; Table 2) increase in age downsection, extending from modern (1956 CE) to nearly 2000 yr B.P. (1942–1827 yr B.P.). In the northern profile group, there are two dates from unit 1 (Fig. 10; Table 2) that are only ~500 yr apart (3173–3005 yr B.P. and 3685–3565 yr B.P.). These dates were from wood and charcoal that were in the same subsample, supporting the reliability of the results. West of the river floor low, dates on unit 1 (Fig. 11; Table 2) increase in age from the top (1178–799 yr B.P.) to the bottom (6482–6317 yr B.P.) of core 21.

There are two dates from unit 3, but neither is reliable; they are shown in red on figures. In core 04 (Figs. 2 and 5; Table 2), a date of 4412–4250 yr B.P. is from material from the top of the unit. This section is quite jumbled and could indicate disturbance post-deposition, allowing for the incorporation of

younger material. In core 20 (Figs. 2 and 9), there is a date from a shell sampled from the top 5 cm and the edge of the core, giving little confidence that it is in situ. The age of 268–14 yr B.P. (Fig. 9; Table 2) would make this unit unreasonably young based on stratigraphic considerations; it is more likely that this shell was pushed down from the surface during the coring process and is not representative of this unit.

■ DISCUSSION

Interpretation of Acoustic and Sedimentary Units

Unit 4 is interpreted to be Pleistocene-aged alluvium or alluvial fan deposits (Atwater and Belknap, 1980; Atwater, 1982; Graymer et al., 2002). This age is supported by the unit's stratigraphic depth and surrounding geology. Except where uplifted, this unit is located ~30 m below sea level, with ~15 m of overlying sediments (Figs. 5–7). On the waterway islands near the study site, undifferentiated alluvial and eolian deposits (Atwater and Belknap, 1980) underlie ~8–20 m of fluvial- and eolian-related sediments, which in turn underlies as much as ~15 m of peat accumulation (Shlemon, 1971; Atwater and Belknap, 1980). The geology onshore south of the study site (~300 m away) is mapped as late Pleistocene alluvial fan deposits (Fig. 14; Graymer et al., 2002). Additionally, the lithology of unit 4 is similar to that of sediment units described by previous work in the eastern Delta and in San Francisco Bay, inferred to have been deposited during early- to mid-glacial times (ca. 70–50 ka; Shlemon, 1972; Atwater et al., 1977; Brown and Pasternack, 2004). After unit 4 was deposited, unconformity 2 formed, probably due to fluvial incision during mid-Wisconsin sea-level fall (ca. 50–38 ka).

Unit 3 is interpreted as channel sediments deposited after formation of unconformity 2, likely between ca. 38 and 7 ka. Atwater and Belknap (1980) documented channel sands unconformably overlying alluvial and eolian sediments just to the east of our study area. The age estimation is despite the date of 4412–4250 yr B.P. from unit 3 in core 04 (Fig. 5). The mixed cobbles and gravels within the sampled unit and the core's location in the river floor low are consistent with disturbance of the shallow portions of unit 3 that caused the incorporation of younger material. The other recent date from unit 3 (268–14 yr B.P.) was likely an artifact of the coring process (Fig. 9).

After deposition of unit 3, the eastern portion of the unit was eroded, creating the more vertical, local unconformity and deepening unconformity 2. Unit 2 was later buttressed against this local unconformity (Figs. 6–7 and 10). The geologic environment of unit 2 is difficult to interpret because its extensions to the north, east, and south are lost to gas wipeout (Figs. 6–7 and 15). Based on the unit's internal stratigraphy and relationship to unit 3, unit 2 is interpreted as subaqueous fan deposits, prograding into a preexisting low. These deposits could be the submerged extension of the Holocene alluvial fan deposits mapped onshore near where New York Slough meets the Sacramento River (Fig. 14; Graymer et al., 2002).

Unconformity 1 likely formed due to small-scale drainage reorganization associated with changing hydrologic conditions between ca. 7 ka and ca. 6.5 ka driven by sea-level and climate fluctuations. Sea-level transgression inundated the Delta sometime between 7 ka (Atwater, 1979) and 6.2 ka (Goman and Wells, 2000). Additionally, regional climate was drier prior to 7 ka and associated with lower water levels in lakes that drain toward the Delta (Malamud-Roam et al., 2006; Negrini et al., 2006). Around 7 ka to 6.5 ka, a transition to a wetter climate caused more frequent river floods and consistent discharge to the Delta (Goman and Wells, 2000; Negrini et al., 2006; Delusina et al., 2022). Channel reorganization and cross-cutting have been documented in the northeastern part of the Delta during this time interval (Brown and Pasternack, 2004). Because the oldest dates from unit 1 in core 21 are close to 6.5 ka (6482–6317 yr B.P.) and there is over a meter of sediment between those dates and unconformity 1, the age of unconformity 1 is inferred to be ca. 7 ka based on regional hydrology and climate.

Estimations of the age of unconformity 1 can also be made from sedimentation rates in unit 1; however, the sedimentation patterns of unit 1 are complex. The sedimentation rates are based on the center of the sample interval and the average of the calibrated age range for each date. Where two dates are from the same subsample, their ages were averaged. The sedimentation rates based on intervals between dates in unit 1 are variable, ranging from ~0.003 to ~0.259 cm/yr. Unit 1 also varies in thickness in the study area, which further increases the range of age estimates based on these rates. For example, in line 40 (Fig. 11), unit 1 is ~2 m thick where core 21 was collected but ~8 m thick a few hundred meters to the north. Age estimates for unconformity 1 at these locations based on the sedimentation rates range from ca. 772 yr ago to ca. 66.67 ka where unit 1 is 2 m thick and ca. 3.09 to ca. 266.67 ka where unit 1 is 8 m thick. Because these estimates are so wide ranging, we prefer the interpretation of ca. 7 ka for the formation of unconformity 1 based on past regional hydrologic considerations.

Unit 1 is interpreted as bay mud (estuarine) deposits of the Holocene. The sands, silts, peats, shells, and other organics (Figs. 5 and 10–11) are typical of this geologic unit where it is mapped in the region (Fig. 14; Atwater, 1979; Atwater and Belknap, 1980; Atwater, 1982; Graymer et al., 2002). Parts of unit 1 have been reworked in modern times, as evidenced by the bedforms observed throughout the study area (Fig. 4).

Controls on River Floor Morphology and Geology

The bathymetry and geology of the Sacramento River in the study area are affected by tectonic and fluvial processes. A marine geologic map based on the chirp data (Fig. 14) denotes surficial units. Most of the area is covered by modern fluvial and estuarine sediments (unit 1), but there are exposures of units 4, 3, and 2. Activity on the Kirby Hills fault at depth has caused broad uplift (more than ~500 m wide in the southern part of the channel) and generated river floor features (e.g., the NNW-SSE ridge, the rounded bank, and the

large-scale fold crests) that have been affected by secondary fluvial processes during and/or post uplift (Fig. 4). For example, the NNE-SSW ridge was uplifted by tectonics, but the sharp scarp on the ridge is due to erosion, as evidenced by the irregular surface of unconformity 2 and a lack of unit 3 on the eastern side of the ridge (Figs. 8 and 9). The bathymetric expression of these features in the southern part of the river channel is due to differential uplift (Figs. 4 and 13), but the exposure of the features in the river floor low, however, is more likely related to fluvial scour preventing their burial. There are swift tidal currents in the area that cause reverse flow of more than 70 cm/s during a flood tide and more than 100 cm/s downstream at ebb (USGS National Water Information System water station 11455478; https://waterdata.usgs.gov/nwis/inventory ?agency_code=USGS&site_no=11455478); these velocities likely limit deposition of mud- to sand-sized grains (Sundborg, 1956). The river floor low is also at the confluence of the Sacramento River and New York Slough and toward the outer bend in the channel (Figs. 2 and 4), both of which could increase local flow velocity and affect erosional and depositional patterns. This is supported by the wide range of sedimentation rates for unit 1 in the study area (~0.003 cm/yr to ~0.259 cm/yr). Such variable sedimentation rates are common in the Delta (Goman and Wells, 2000; Maier et al., 2015), but rates on the higher end are less common. Modern sedimentation may be affected by the regional shipping channels, which are routinely dredged (for bathymetric changes associated with dredging, see https://www.spn.usace.army.mil/Missions/Surveys -Studies-Strategy/Hydro-Survey/Sacramento-River-Deep-Water-Ship-Channel/ and https://www.spn.usace.army.mil/Missions/Surveys-Studies-Strategy/Hydro -Survey/Suisun-Bay-Channel/). The study area is between the Sacramento River Deep Water shipping channel, the Suisun Bay shipping channel, and the New York Slough shipping channel, which extends to the edge of the low in the Sacramento River floor (National Oceanic and Atmospheric Administration (NOAA) Office of Coast Survey, 2010; Fig. 4). The river floor low is not actively dredged, but it is possible that prior human activities, such as hydraulic mining, contributed to the sharp bathymetric drop from New York Slough into the low. Gas in the sediments of New York Slough makes it difficult to determine the stratigraphic relationships across this sharp drop. Regional cables, pipes, and other modern anthropogenic infrastructure also contribute to river floor morphology (Fig. 9). Finally, the tidal currents in the region also form the sediment bedforms of varying scales on the river floor (Fig. 4). Most are asymmetric from the dominant downstream flow direction.

Interpretation of Fault-Related Deformation and Age Constraints

The traces of the Kirby Hills fault crossing the Sacramento River shown on the figures (Figs. 1–10) are from the USGS Quaternary fault and fold database (USGS and CGS, 2020) and are mapped based on lower vertical-resolution and deeper-penetration seismic data that image the fault zone at depth. The western inflection point, denoting the onset of fold deformation, is mapped in the chirp data between 0 and 100 m to the east of the easternmost USGS

fault strand (Fig. 13A), supporting the near-vertical structure of the fault with a slight westward dip (Parsons et al., 2002). We do not observe any evidence of the western fault strand as previously mapped. However, there is a series of gas wipeouts in the chirp data, located ~100 m to the west of this fault strand (Figs. 6, 8, 10, and 13A). These could be related to gas rising from a fault plane deeper than is imaged in our chirp data. Alternatively, these gas wipeouts could be unrelated to faulting, given that subsurface gas is very common in this region (California Department of Conservation, Geologic Energy Management Division, 2022).

The closely spaced chirp profiles across the Kirby Hills fault zone highlight how much the expression of fault-related folding can vary over a short distance (Fig. 12), and they capture the complex stratigraphic sequences generated by the interplay of fault activity and erosional and depositional processes. The overall change in character of folding related to activity on the Kirby Hills fault at depth along with the relative change in uplift across the river channel indicate that the fault tip is plunging to the northwest (Figs. 12 and 13). Differential erosion may also explain some of the differences in deformation character along the fault.

During deposition of unit 4 in the Pleistocene, fault-related deformation was ongoing, indicated by truncated reflectors in the western part of the unit in the southern and central profile groups that thin onto the fold (Figs. 5, 6, and 8).

There was fault-related folding during and after deposition of unit 3 in the southern profile group (Figs. 8 and 9) based on reflector patterns at the monocline. The central group chirp profiles (Figs. 5 and 6), where the folded material is exposed at the river floor, have stratigraphy that indicates uplift of unit 3 during or after deposition, but a pure depositional origin of some of these geometries cannot be ruled out. Unit 3 east of the fold, specifically, is difficult to interpret because the reflection geometry is imaged poorly where it meets unconformity 2 due to limitations of the chirp beam width when crossing a rounded feature. Unit 3 in the northern group (Fig. 10) is not imaged well enough to interpret the presence of deformation.

After deposition of unit 3, there was a drainage reorganization that eroded away parts of unit 3 and further incised unconformity 2 in the area of the central and northern profile groups (Figs. 6, 7, 10, and 15). This is based on the absence of unit 3 below unit 2 and the drop in unconformity 2 where unit 2 is present (Figs. 6, 7, 10, and 15). This could have been related to natural fluvial processes, but differential uplift across the channel from the plunging fold probably played a role, given that more uplift in the south would have focused water toward the north (Fig. 13B). Unit 2 was deposited after this, filling in the lows in unconformity 2 and abutting unit 3.

Unit 1 exhibits no obvious fault-related folding in the study area, indicating that folding related to motion on the Kirby Hills fault at depth has not propagated to the surface since the formation of unconformity 1, ca. 7 ka. However, the internal character of the unit is primarily chaotic with discontinuous reflectors, which could conceal evidence of deformation; or, any such evidence could have been reworked by currents, which have generated nearby bedforms that are as much as 1.5 m in height. Dates that are likely representative of
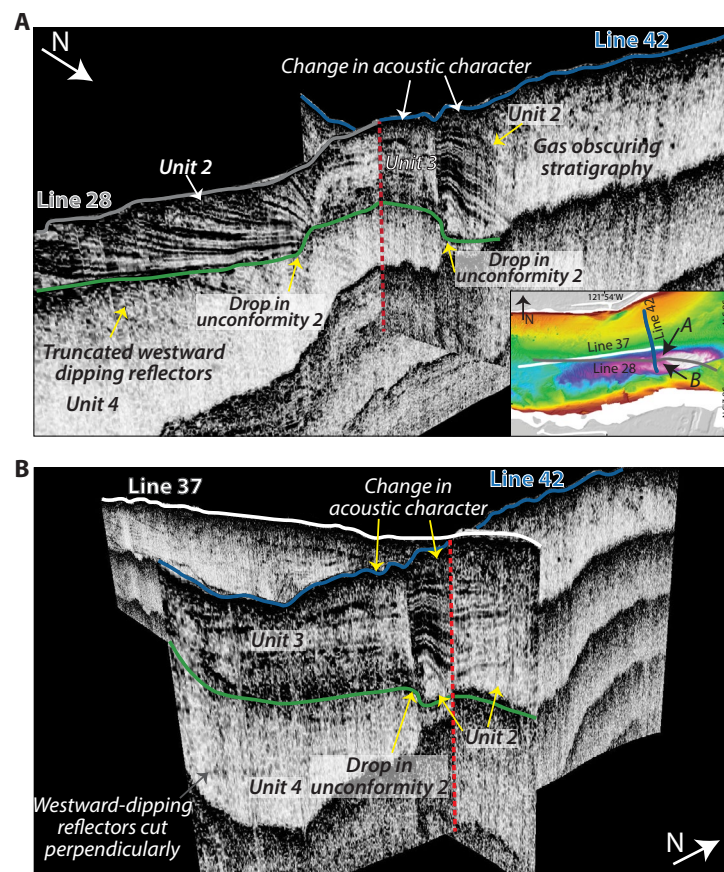
Figure 15. Perspective views of a fault-like stratigraphic pattern that is of fluvial origin. Chirp profiles shown and view directions are on inset, denoted by colored lines and arrows, respectively. For additional bathymetry context (colors in inset), see Figure 2. Line 28 is also shown in Figure 7, and line 37 is also shown in Figure 10. Vertical exaggeration is 6×.

depositional age in the northern and central profile groups provide constraints on the minimum age of surface folding. This is ca. 3000 years ago in the northern group and ca. 1600 years ago in the central group (Figs. 5 and 10; Table 2).

Unit 1 is of minimal spatial extent in the southern profile group, so there is a lack of age constraints (Figs. 8, 9, and 14). It is possible that post-transgression uplift in the south prevented deposition of unit 1 and led to erosion of unit 1 sediments that may have been previously deposited. The broader zone of folding, general divergence from north to south of the points of inflection in the monocline, and higher uplift and increased folding of unit 3 relative to the rest of the channel to the north (Figs. 12 and 13) could support this. If there was

post-transgression folding in the southern group, the youngest deformation probably occurred more than 150 years ago, given that there was no surface deformation for the 1889 M 6 earthquake that occurred in the vicinity of Pittsburg and Antioch (Keeler, 1890; Weber-Band et al., 1997; Wong et al., 1988); however, it is possible that there was some surface deformation that was not noticed or reported. Overall, in the southern portion of the Sacramento River, there are larger-scale deformation that diminishes northward across the channel and potential evidence of more recent activity, but nothing that conclusively supports shallow folding in the past 7 k.y. associated with the Kirby Hills fault.

Seismicity data since 1969 (Northern California Earthquake Data Center, 2014; Fig. 3) show that many earthquakes have occurred within the study area, but most were smaller than M 3 and quite deep (>15 km). South of the river channel, seismicity trends toward the southeast, following the curve of the previously mapped eastern strand of the Kirby Hills fault. This trend is also seen in the chirp data, where there is a slight eastern shift in deformation to the south (i.e., eastern point of inflection, NNW-SSE ridge; Figs. 4 and 13), but gaseous sediments and data extent limit the robustness of this signal (Figs. 8 and 9). Previous work has proposed that the Kirby Hills fault links up to the Kirker fault in the south (Figs. 1 and 3; Krug et al., 1992; Parsons et al., 2002; Unruh et al., 2007; Unruh and Hitchcock, 2009). This may be the case, but the shallow stratigraphic data do not appear to follow this S-SW trajectory and instead have a more NW-SE trend, extending toward the Antioch fault (Figs. 3 and 13).

Difficulties with Paleoseismology in an Anthropogenically Modified Fluvial Environment

Interpretation of stratigraphic features in this type of study area is complex and requires an abundance of data to fully characterize the imaged structures. There are many features that could have either tectonic or depositional origins, and interpretation of such features one way or the other has implications for seismic hazard assessment (Perea et al., 2018; Wei et al., 2020). One prime example of this type of tectonic versus depositional ambiguity is an apparent fault imaged in chirp line 42, which crosses the river floor low (Fig. 15). In this profile, unconformity 2 has an abrupt drop down to the north. The overlying sediments on the southern side are relatively flat lying without much internal layering (unit 3). The sediments above the unconformity on the northern side are layered with high acoustic amplitude and have a curved dip to them (unit 2). This distinct change in acoustic character is associated with the drop in unconformity 2, suggestive of a fault offset. However, based on correlation with intersecting lines, this feature is more likely associated with fluvial erosion and subsequent deposition. Yet, the location of fluvial erosion was probably influenced by motion on the Kirby Hills fault, which has uplifted unconformity 2 higher on the south side of the river channel as compared to the north (Fig. 13B). This uplifted area would have altered water flow, focusing it into the deeper, northern part of the channel. This likely caused erosion of

the eastern portion of unit 3 and additional erosion of unit 4, further lowering unconformity 2, but was followed by deposition of unit 2, filling in this low. The sharp, fault-like stratigraphic boundary is related to deposition of two separate sediment packages driven by tectonic activity but is not a fault strand itself, just a local unconformity. Such tectonic controls on drainage morphology are common (Graves et al., 2021; Klotsko et al., 2021). Anthropogenic features, like shipping channels, can also have fault-like morphologies (Singleton et al., 2021). The edges of a shipping channel resemble seafloor scarps formed via fault activity (Klotsko et al., 2015; Brothers et al., 2020), and sediments that infill the dredge channels abut the channel wall, forming a sharp stratigraphic boundary (Singleton et al., 2021). These sediments can even dip toward the boundary (Singleton et al., 2021), as is common in fault-related deformation (Watt et al., 2016; Singleton et al., 2021). Interpreting data in these types of areas can be further complicated by strong currents, which can cause resuspension and deposition of sediments, potentially removing evidence of fault motion (Sahakian et al., 2022). These and other factors need to be considered when studying fluvial environments, particularly those in areas modified by humans.

This study also highlights the challenges of submarine geologic sampling for paleoseismology in a fluvial environment. This work was conducted in an anthropogenically modified area, in a river with high tidal flux and active regional dredging. These conditions are not conducive to preserving the highest-quality sediment and seismic records for investigating past fault activity. Environments that are more isolated and with lower energy, such as the marine realm (Barnes and Pondard; 2010; Brothers et al., 2020; Perea et al., 2021), lakes (Brothers et al., 2009; Maloney et al., 2013), and embayments (Watt et al., 2016; Watt et al., 2022), allow for a more continuous sediment record, which is ideal for such studies. Nevertheless, collecting any data with the potential to gain knowledge about poorly constrained faults is worthwhile, but future researchers working in such fluvial systems should be aware of the potential limitations. In terms of geophysical data collection, subsurface data are generally of higher quality with fuller coverage and faster to collect in a fluvial system than on land and are ideal for an urban region, where human infrastructure and land use can obscure the geomorphic expression of fault activity. Yet, when compared to other aquatic environments, rivers may be relatively shallow, causing data artifacts that obscure real stratigraphy; there can be physical obstructions that prevent surveying, such as large ships and bridge pylons; tides can affect the data collection process; and if a fault crosses a channel perpendicularly, only a short section of the fault can be mapped. Fluvial systems also have complex sedimentation patterns. Sediments from upstream and the surrounding landscape that are deposited in a fluvial or delta environment can contain material with inherited ages. This mixing of sediments can result in a highly variable age record, making interpretations difficult (Sahakian et al., 2022). In urban rivers, dredging, waterside development, outflow pipes, cables (Fig. 9), and other anthropogenic modifications can disrupt the sediment record, further complicating interpretations, especially spatially, given that these disruptions are not uniform over an entire area. Despite these limitations, valuable information about seismic hazards can be garnered from paleoseismic interpretation of subsurface data collected in a fluvial environment.

■ CONCLUSIONS

The character of shallow deformation caused by the buried Kirby Hills fault varies over a lateral distance of ~600 m where it crosses the Sacramento River. The main (eastern) strand of the fault is associated with a monocline in west-dipping sediment that plunges to the northwest, supported by more uplift in the southern part of the river. This is expressed surficially by a NNW-SSE ridge and other mounded features. Points of inflection in the monocline primarily diverge from north to south, consistent with the broadening zone of uplifted and deformed strata imaged in the chirp data. Despite deformation of the river floor, there is not enough evidence to support shallow folding caused by the Kirby Hills fault at depth in the past ~7 k.y. There are minimum constraints on the age of last deformation in the northern, central, and southern areas of ca. 3000 yr B.P., ca. 1600 yr B.P., and 150 yr ago, respectively. Additional data collection is needed to better constrain the deformation history of this area. The previously mapped western strand of the Kirby Hills fault that crosses the Sacramento River does not exhibit near-surface deformation, but gas may be rising from the fault at depth.

The results of this study show the value of closely spaced subbottom profiles, given that fault-related deformation can vary greatly over short distances. This project also highlights how conducting a paleoseismologic study in a fluvial system comes with added difficulties relative to a deeper and/or more isolated aquatic study site, especially in terms of stratigraphic interpretations and chronology, but valuable information can still be gained from such studies. Fluvial surveys are particularly useful in urbanized areas where human modification hinders onshore fault investigations; they also provide more continuous coverage than is attainable onshore.

REFERENCES CITED

Atwater, B.F., 1979, Ancient processes at the site of southern San Francisco Bay, movement of the crust and changes in sea level, *in* Conomos, T.J., ed., San Francisco Bay: The Urbanized

Estuary: Investigations into the Natural History of San Francisco Bay and Delta with Reference to the Influence of Man: Fifty-Eighth Annual Meeting of the Pacific Division/American Association for the Advancement of Science: San Francisco, American Association for the Advancement of Science Pacific Division, p. 31–45.

Atwater, B.F., 1982, Geologic maps of the Sacramento–San Joaquin Delta, California: U.S. Geological Survey Miscellaneous Field Studies Map 1401, 21 sheets, scale 1:24,000, with 15 p. text, https://doi.org/10.3133/mf1401.

Atwater, B.F., and Belknap, D.F., 1980, Tidal-wetland deposits of the Sacramento–San Joaquin Delta, California, in Field, M.E., Buoma, A.H., Coburn, I.P., Douglas, R.G., and Ingle, J.C., eds., Pacific Coast Paleogeography Symposium 4: Quaternary Depositional Environments of the Pacific Coast: Pacific Section, Society of Economic Paleontologists and Mineralogists, p. 89–103.

Atwater, B.F., Hedel, C.W., and Helley, E.J., 1977, Late Quaternary depositional history, Holocene sea-level changes, and vertical crustal movement, southern San Francisco Bay, California: U.S. Geological Survey Professional Paper 1014, 15 p., https://doi.org/10.3133/pp1014.

Atwater, T., 1970, Implications of plate tectonics for the Cenozoic tectonic evolution of western North America: Geological Society of America Bulletin, v. 81, p. 3513–3536, https://doi.org/10.1130/0016-7606(1970)81[3513:IOPTFT]2.0.CO;2.

Barnes, P.M., and Pondard, N., 2010, Derivation of direct on-fault submarine paleoearthquake records from high-resolution seismic reflection profiles: Wairau Fault, New Zealand: Geochemistry, Geophysics, Geosystems, v. 11, Q11013, https://doi.org/10.1029/2010GC003254.

Bronk Ramsey, C., 2009, Bayesian analysis of radiocarbon dates: Radiocarbon, v. 51, p. 337–360, https://doi.org/10.1017/S0033822200033865.

Brothers, D.S., Kent, G.M., Driscoll, N.W., Smith, S.B., Karlin, R., Dingler, J.A., Harding, A.J., Seitz, G.G., and Babcock, J.M., 2009, New constraints on deformation, slip rate, and timing of the most recent earthquake on the West Tahoe–Dollar Point fault, Lake Tahoe Basin, California: Bulletin of the Seismological Society of America, v. 99, p. 499–519, https://doi.org/10.1785/0120080135.

Brothers, D.S., Miller, N.C., Barrie, J.V., Haeussler, P.J., Greene, H.G., Andrews, B.D., Zielke, O., Watt, J., and Dartnell, P., 2020, Plate boundary localization, slip-rates and rupture segmentation of the Queen Charlotte Fault based on submarine tectonic geomorphology: Earth and Planetary Science Letters, v. 530, https://doi.org/10.1016/j.epsl.2019.115882.

Brown, K.J., and Pasternack, G.B., 2004, The geomorphic dynamics and environmental history of an upper deltaic floodplain tract in the Sacramento–San Joaquin Delta, California, USA: Earth Surface Processes and Landforms, v. 29, p. 1235–1258, https://doi.org/10.1002/esp.1088.

CALFED Bay-Delta Program, 2000, Programmatic record of decision: CALFED Bay-Delta Program, 118 p.

California Department of Conservation, Geologic Energy Management Division, 2022, Boundaries and associated data for oil and gas fields, https://gis.conservation.ca.gov/portal/home/item.html?id=6ce75e7d9f66435781cb15fdb3cca36a (data accessed 28 December 2022).

Cherven, V.B., 1983, Mesozoic through Paleogene evolution of the Sacramento Basin, California, in Cherven, V.B., and Graham, S.A., eds., Geology and Sedimentology of the Southwestern Sacramento Basin and East Bay Hills: Pacific Section, Society of Economic Paleontologists and Mineralogists, p. 21–31.

Childs, J.R., Hart, P., Bruns, T.R., Marlow, M.S., and Sliter, R., 2000, High-resolution marine seismic reflection data from the San Francisco Bay area: U.S. Geological Survey Open-File Report 00-494, https://doi.org/10.3133/ofr00494.

Cohen, J.K., and Stockwell, J.W., Jr., 2015, CWP/SU: Seismic Unix Release No. 44: An open source software package for seismic research and processing, Center for Wave Phenomena, Colorado School of Mines.

Dasler, J., 2000, Hydrographic survey H10897: https://www.ngdc.noaa.gov/nos/H10001-H12000/H10897.html (accessed January 2018).

Delta Stewardship Council, 2013, Introduction, in The Delta Plan: Sacramento, California, Delta Stewardship Council, p. 1–24, https://deltacouncil.ca.gov/delta-plan/ (accessed September 2016).

Delusina, I., Starratt, S.W., and Verosub, K.L., 2022, Environmental evolution of peat in the Sacramento–San Joaquin Delta (California) during the Middle and Late Holocene as deduced from pollen, diatoms and magnetism: Quaternary International, v. 621, p. 50–61, https://doi.org/10.1016/j.quaint.2020.05.012.

Fletcher, J.B., and Erdem, J., 2017, Shear-wave velocity model from Rayleigh wave group velocities centered on the Sacramento/San Joaquin Delta: Pure and Applied Geophysics, v. 174, p. 3825–3839, https://doi.org/10.1007/s00024-017-1587-x.

Fletcher, J.B., Erdem, J., Seats, K., and Lawrence, J., 2016, Tomographic Rayleigh wave group velocities in the Central Valley, California, centered on the Sacramento/San Joaquin Delta:

Journal of Geophysical Research: Solid Earth, v. 121, p. 2429–2446, https://doi.org/10.1002/2015JB012376.

Goman, M., and Wells, L., 2000, Trends in river flow affecting the northeastern reach of the San Francisco Bay estuary over the past 7000 years: Quaternary Research, v. 54, p. 206–217, https://doi.org/10.1006/qres.2000.2165.

Graves, L.G., Driscoll, N.W., and Maloney, J.M., 2021, Tectonic and eustatic control on channel formation, erosion, and deposition along a strike-slip margin, San Diego, California, USA: Continental Shelf Research, v. 231, https://doi.org/10.1016/j.csr.2021.104571.

Graymer, R.W., Jones, D.L., and Brabb, E.E., 2002, Geologic map and map database of northeastern San Francisco Bay region, California: U.S. Geological Survey Miscellaneous Field Studies Map 2403, scale 1:100,000, https://doi.org/10.3133/mf2403.

Graymer, R.W., Bryant, W., McCabe, C.A., Hecker, S., and Prentice, C.S., 2006, Map of Quaternary-active faults in the San Francisco Bay region: U.S. Geological Survey Scientific Investigations Map 2919, scale 1:275,000, https://doi.org/10.3133/sim2919.

Horton, J.D., San Juan, C.A., and Stoeser, D.B., 2017, The State Geologic Map Compilation (SGMC) geodatabase of the conterminous United States: U.S. Geological Survey Data Series 1052, 46 p., https://doi.org/10.3133/ds1052.

Hua, Q., Barbetti, M., and Rakowski, A.J., 2013, Atmospheric radiocarbon for the period 1950–2010: Radiocarbon, v. 55, p. 2059–2072, https://doi.org/10.2458/azu_js_rc.v55i2.16177.

Ingebritsen, S.E., and Ikehara, M.E., 1999, Sacramento–San Joaquin Delta: The sinking of the heart of the state, in Galloway, D., Jones, D.R., and Ingebritsen, S.E., eds., Land Subsidence in the United States: U.S. Geological Survey Circular 1182, p. 83–94, https://doi.org/10.3133/cir1182.

Keeler, J.E., 1890, Earthquakes in California in 1889: U.S. Geological Survey Bulletin 68, 25 p., https://doi.org/10.3133/b68.

Klotsko, S., Driscoll, N., Kent, G., and Brothers, D., 2015, Continental shelf morphology and stratigraphy offshore San Onofre, California: The interplay between rates of eustatic change and sediment supply: Marine Geology, v. 369, p. 116–126, https://doi.org/10.1016/j.margeo.2015.08.003.

Klotsko, S., Skakun, M., Maloney, J., Gusick, A., Davis, L., Nyers, A., and Ball, D., 2021, Geologic controls on paleodrainage incision and morphology during sea level lowstands on the Cascadia shelf in Oregon, USA: Marine Geology, v. 434, https://doi.org/10.1016/j.margeo.2021.106444.

Krug, E.H., Cherven, V.B., Hatten, C.W., and Roth, J.C., 1992, Subsurface structure in the Montezuma Hills, southwestern Sacramento Basin, in Cherven, V.B., and Edmondson, W.F., eds., Structural Geology of the Sacramento Basin: Pacific Section American Association of Petroleum Geologists Miscellaneous Publication 41, p. 41–60.

Lund, J., Hanak, E., Fleenor, W., Howitt, R., Mount, J., and Moyle, P., 2007, Envisioning futures for the Sacramento–San Joaquin Delta: San Francisco, Public Policy Institute of California, 325 p.

MacKevett, N.H., 1992, The Kirby Hill Fault Zone, in Cherven V.B., and Edmondson, W.F., eds., Structural Geology of the Sacramento Basin: Pacific Section American Association of Petroleum Geologists Miscellaneous Publication 41, p. 61–78.

Maier, K.L., Gatti, E., Wan, E., Ponti, D.J., Pagenkopp, M., Starratt, S.W., Olson, H.A., and Tinsley, J.C., 2015, Quaternary tephrochronology and deposition in the subsurface Sacramento–San Joaquin Delta, California, USA: Quaternary Research, v. 83, p. 378–393, https://doi.org/10.1016/j.yqres.2014.12.007.

Malamud-Roam, F.P., Ingram, L.B., Hughes, M., and Florsheim, J.L., 2006, Holocene paleoclimate records from a large California estuarine system and its watershed region: Linking watershed climate and bay conditions: Quaternary Science Reviews, v. 25, p. 1570–1598, https://doi.org/10.1016/j.quascirev.2005.11.012.

Maloney, J.M., Noble, P.J., Driscoll, N.W. Kent, G.M., Smith, S.B., Schmauder, G.C., Babcock, J.M., Baskin, R.L., Karlin, R., Kell, A.M., Seitz, G.G., Zimmerman, S., and Kleppe, J.A., 2013, Paleoseismic history of the Fallen Leaf segment of the West Tahoe–Dollar Point fault reconstructed from slide deposits in the Lake Tahoe Basin, California-Nevada: Geosphere, v. 9, p. 1065–1090, https://doi.org/10.1130/GES00877.1.

Mount, J., and Twiss, R., 2005, Subsidence, sea level rise, seismicity in the Sacramento–San Joaquin Delta: San Francisco Estuary and Watershed Science, v. 3, no. 1, https://doi.org/10.15447/sfews.2005v3iss1art7.

National Oceanic and Atmospheric Administration (NOAA) Office of Coast Survey, 2010, Suisun Bay, NOAA Chart 18565, 56th edition, scale 1:40,000, https://charts.noaa.gov/PDFs/18656.pdf.

Northern California Earthquake Data Center, 2014, Northern California Earthquake Data Center: University of California Berkeley Seismological Laboratory, https://ncedc.org/ncedc_doi_metadata.html.

Klotsko et al. | Kirby Hills fault

Negrini, R.M., Wigand, P.E., Draucker, S., Gobalet, K., Gardner, J.K., Sutton, M.Q., and Yohe, R.M., II, 2006, The Rambla highstand shoreline and the Holocene lake-level history of Tulare Lake, California, USA: Quaternary Science Reviews, v. 25, p. 1599–1618, https://doi.org/10.1016/j.quascirev.2005.11.014.

Pagano, L., 2012, Hydrographic survey H12340: https://www.ngdc.noaa.gov/nos/H12001-H14000/H12340.html (last accessed January 2018).

Parsons, T., McCarthy, J., Hart, P.E., Hole, J.A., Childs, J., Oppenheimer, D.H., and Zoback, M.L., 2002, A review of faults and crustal structure in the San Francisco Bay area as revealed by seismic studies, in Parsons, T.E., ed., Crustal Structure of the Coastal and Marine San Francisco Bay Region, California: U.S. Geological Survey Professional Paper 1658, p. 119–145, https://doi.org/10.3133/pp1658.

Perea, H., Gràcia, E., Martínez-Loriente, S., Bartolomé, R., Gómez de la Peña, L., de Mol, B., Moreno, X., Lo Iacono, C., Diez, S., Tello, O., Gómez-Ballesteros, M., and Dañobeitia, J.J., 2018, Kinematic analysis of secondary faults within a distributed shear-zone reveals fault linkage and increased seismic hazard: Marine Geology, v. 399, p. 23–33, https://doi.org/10.1016/j.margeo.2018.02.002.

Perea, H., Ucarkus, G., Driscoll, N., Kent, G., Levy, Y., and Rockwell, T., 2021, Faulting and folding of the Transgressive Surface offshore Ventura records deformational events in the Holocene: Frontiers of Earth Science, v. 9, https://doi.org/10.3389/feart.2021.655339.

Reimer, P.J., Austin, W.E.N, Bard, E., Bayliss, A., Blackwell, P.G., Bronk Ramsey, C., Butzin, M., Cheng, H., Edwards, R.L., Friedrich, M., Grootes, P.M., Guilderson, T.P., Hajdas, I., Heaton, T.J., Hogg, A.G., Hughen, K.A., Kromer, B., Manning, S.W., Muscheler, R., Palmer, J.G., Pearson, C., van der Plicht, J., Reimer, R.W., Richards, D.A., Scott, E.M., Southon, J.R., Turney, C.S.M., Wacker, L., Adolphi, F., Büntgen, U., Capano, M., Fahrni, S.M., Fogtmann-Schulz, A., Friedrich, R., Köhler, P., Kudsk, S., Miyake, F., Olsen, J., Reinig, F., Sakamoto, M., Sookdeo, A., and Talamo, S., 2020, The IntCal20 Northern Hemisphere radiocarbon age calibration curve (0–55 cal kBP): Radiocarbon, v. 62, p. 725–757, https://doi.org/10.1017/RDC.2020.41.

Reimer, R.W., and Reimer, P.J., 2022, CALIBomb: http://calib.org (accessed 11 July 2022).

Sahakian, V.J., Derosier, B.J., Rockwell, T.K., and Stock, J.M., 2022, Shallow distributed faulting in the Imperial Valley, California, USA: Geology, v. 50, p. 626–630, https://doi.org/10.1130/G49572.1.

Shlemon, R.J., 1971, The Quaternary deltaic and channel system in the central Great Valley, California: Annals of the Association of American Geographers, v. 61, p. 427–440, https://doi.org/10.1111/j.1467-8306.1971.tb00797.x.

Shlemon, R.J., 1972, The lower American River area, California: A model of Pleistocene landscape evolution: Yearbook of the Association of Pacific Coast Geographers, v. 34, p. 61–86, https://doi.org/10.1353/pcg.1972.0001.

Singleton, D.M., Maloney, J.M., Brothers, D.S., Klotsko, S., Driscoll, N.W., and Rockwell, T.K., 2021, Recency of faulting and subsurface architecture of the San Diego Bay pull-apart basin, California, USA: Frontiers of Earth Science, v. 9, https://doi.org/10.3389/feart.2021.641346.

Stuiver, M., and Polach, H.A., 1977, Discussion reporting of 14C data: Radiocarbon, v. 19, p. 355–363, https://doi.org/10.1017/S0033822200003672.

Suddeth, R.J., Mount, J., and Lund, J.R., 2010, Levee decisions and sustainability for the Sacramento–San Joaquin Delta: San Francisco Estuary and Watershed Science, v. 8, no. 2, https://doi.org/10.15447/sfews.2010v8iss2art3.

Sundborg, Å., 1956, The river Klarälven: A study of fluvial processes: Geografiska Annaler, v. 38, p. 238–316, https://doi.org/10.2307/520285.

Thurber, C., Zhang, H.J., Brocher, T., and Langenheim, V., 2009, Regional three-dimensional seismic velocity model of the crust and uppermost mantle of northern California: Journal of Geophysical Research, v. 114, B01304, https://doi.org/10.1029/2008JB005766.

Unruh, J.R., and Hitchcock, C.S., 2009, Characterization of potential seismic sources in the Sacramento–San Joaquin Delta, California: Final technical report: U.S. Geological Survey National Earthquake Hazards Reduction Program, award 08HQGR0055, 45 p.

Unruh, J.R., and Sundermann, S., 2006, Digital compilation of thrust and reverse fault data for the Northern California Map Database: Collaborative research with William Lettis & Associates, Inc., and the U.S. Geological Survey: U.S. Geological Survey National Earthquake Hazards Reduction Program, award 05HQGR0054, 24 p.

Unruh, J.R., Dumitru, T.A., and Sawyer, T.L., 2007, Coupling of early Tertiary extension in the Great Valley forearc basin with blueschist exhumation in the underlying Franciscan accretionary wedge at Mount Diablo, California: Geological Society of America Bulletin, v. 119, p. 1347–1367, https://doi.org/10.1130/B26057.1.

USGS (U.S. Geological Survey), 2020, Station 11455478: Sacramento R A Decker Island NR Rio Vista CA: National Water Information System, https://waterdata.usgs.gov/nwis/inventory?agency_code=USGS&site_no=11455478 (accessed December 2020).

USGS (U.S. Geological Survey) and CGS (California Geological Survey), 2020, Quaternary fault and fold database for the United States, https://www.usgs.gov/natural-hazards/earthquake-hazards/faults (accessed August 2020).

Watt, J., Ponce, D., Parsons, T., and Hart, P., 2016, Missing link between the Hayward and Rodgers Creek faults: Science Advances, v. 2, https://doi.org/10.1126/sciadv.1601441.

Watt, J.T., McGann, M.L., Takesue, R.K., and Lorenson, T.D., 2022, Marine paleoseismic evidence for seismic and aseismic slip along the Hayward-Rodgers Creek fault system in northern San Pablo Bay: Geochemistry, Geophysics, Geosystems, v. 23, https://doi.org/10.1029/2021GC010180.

Weber-Band, J., Williams, P.L., Jones, D.L., Johnson, P.S., and McEvilly, T.V., 1997, Active tectonic deformation at the eastern margin of the California Coast Ranges: Results of the BASIX and CALCRUST programs: U.S. Geological Survey Open-File Report 97-691, 17 p., https://doi.org/10.3133/ofr97691.

Wei, E.A., Holmes, J.J., and Driscoll, N.W., 2020, Strike-slip transpressional uplift offshore San Onofre, California inhibits sediment delivery to the deep sea: Frontiers of Earth Science, v. 8, 51, https://doi.org/10.3389/feart.2020.00051.

WGCEP (Working Group on California Earthquake Probabilities) Thrust Fault Subgroup, 1999, Report to the Working Group on Northern California Earthquake Probabilities: Southern California Earthquake Center, 15 p.

Wong, I.G., Ely, R.W., and Kollmann, A.C., 1988, Contemporary seismicity and tectonics of the northern and central Coast Ranges–Sierran block boundary zone, California: Journal of Geophysical Research, v. 93, p. 7813–7833, https://doi.org/10.1029/JB093iB07p07813.

Young, M., 2019, Geologic investigation of the Kirby Hills fault along the Sacramento River [B.S. thesis]: San Diego, California, San Diego State University, 12 p.